https://doi.org/10.5194/egusphere-2025-4326
Preprint. Discussion started: 24 September 2025

The impact of aerosol mixing state on immersion freezing: Insights from classical nucleation theory and particle-resolved simulations

Wenhan Tang[1], Sylwester Arabas[2], Jeffrey H. Curtis[1], Daniel A. Knopf[3], Matthew West[4], and Nicole Riemer[1]

[1]Department of Climate, Meteorology, and Atmospheric Sciences, University of Illinois Urbana-Champaign, Urbana, Illinois, USA
[2]Faculty of Physics and Applied Computer Science, AGH University of Krakow, Kraków, Poland
[3]School of Marine and Atmospheric Sciences, Stony Brook University, Stony Brook, New York, USA
[4]Department of Mechanical Science and Engineering, University of Illinois Urbana-Champaign, Urbana, Illinois, USA

Correspondence: Wenhan Tang (wenhant2@illinois.edu) and Nicole Riemer (nriemer@illinois.edu)

Abstract. Immersion freezing, initiated by ice-nucleating particles (INPs) in supercooled aqueous droplets, plays an important role in the formation of ice crystals within clouds. The efficiency of immersion freezing depends strongly on INP composition and, crucially, on the mixing state—how chemical species are distributed across the particle population. Here, we quantify the impact of aerosol mixing state on immersion freezing using a combined theoretical and particle-resolved modeling approach. We derive analytical expressions for the frozen fraction of internally and externally mixed INP populations based on classical nucleation theory, showing that the frozen fraction is sensitive to whether ice-active species are present in all particles or only in a subset of the population. We introduce a multi-species immersion freezing scheme into the particle-resolved model PartMC, using the water activity-based immersion freezing model (ABIFM) to compute freezing probabilities for mixed-composition particles. To improve computational efficiency, we implement a Binned Tau-Leaping algorithm and demonstrate an order-of-magnitude speedup with minimal accuracy loss. Simulations confirm the theoretical prediction that internally mixed populations yield higher frozen fractions than externally mixed ones under otherwise identical conditions. Sensitivity analyses across particle size, species type, and cooling condition reveal that the mixing state effect is most pronounced when small amounts of highly efficient INPs are mixed with less efficient materials. These findings underscore the need to represent aerosol mixing state explicitly in models of heterogeneous ice nucleation to reduce uncertainty in cloud-phase partitioning.

1 Introduction

Atmospheric aerosols are complex mixtures of different chemical species, a characteristic driven by their diverse sources and aging processes during transport. This phenomenon has been extensively studied through both field and laboratory observations (e.g., Andreae and Crutzen, 1997; Murphy and Thomson, 1997; Rudich, 2003; Zhang et al., 2007; Baustian et al., 2012; Laskin et al., 2016; Hodshire et al., 2019; Laskin et al., 2019; Lata et al., 2021; Shao et al., 2022). Aerosol mixing state varies along a spectrum from externally mixed to internally mixed populations. In an external mixture, each particle consists of a single chemical species, whereas in an internal mixture, all particles share the same composition (Winkler, 1973). The mixing state

https://doi.org/10.5194/egusphere-2025-4326
Preprint. Discussion started: 24 September 2025

of aerosols impacts their climate-relevant properties including cloud condensation nuclei (CCN) activity (Deng et al., 2013; Ren et al., 2018; Wang et al., 2018; Rejano et al., 2024) and aerosol optical properties (e.g., Lesins et al., 2002; Ma et al., 2011, 2012; Liu and Mishchenko, 2018; Stevens and Dastoor, 2019; Zheng et al., 2021). However, its impact on heterogeneous ice nucleation remains comparatively underexplored, a gap that this study aims to address.

Ice nucleating particles (INPs) are aerosol particles that facilitate ice crystal formation by lowering the energy barrier for ice nucleation (Pruppacher and Klett, 1979; Knopf and Alpert, 2023). This process allows ice to form at higher temperatures than would be possible through homogeneous nucleation. INPs play a critical role in mixed-phase clouds by altering the water-to-ice content ratio, thereby influencing both cloud glaciation and precipitation formation (Pruppacher and Klett, 1979; Lohmann, 2002; Ansmann et al., 2008; Kanji et al., 2017; Storelvmo, 2017). This modulation of the water-to-ice content ratio also affects radiative transfer within mixed-phase clouds (McCoy et al., 2014a, b, 2016; Murray et al., 2021), which is a key factor in regulating the Earth's radiative balance.

Numerous studies highlight the importance of aerosol chemical composition in heterogeneous ice nucleation (e.g., Möhler et al., 2008; Phillips et al., 2008; Knopf et al., 2018; Joghataei et al., 2020). The chemical and physical properties of aerosol species, such as their surface structure, surface chemistry, and hydrophilicity or hydrophobicity, strongly influence their effectiveness as INPs (Diehl and Mitra, 1998; Zuberi et al., 2002; Knopf et al., 2014; Fitzner et al., 2015; Bi et al., 2016; Wang et al., 2016; Kiselev et al., 2017; Yang et al., 2018). Different species exhibit highly variable heterogeneous ice nucleation rates, spanning several orders of magnitude under identical environmental conditions (Diehl and Mitra, 1998; Murray et al., 2012; Knopf and Alpert, 2013; Kanji et al., 2017; Knopf et al., 2018; Wagner et al., 2021). Since the mixing state determines how chemical species with varying ice nucleation efficiencies are distributed within an aerosol population, it plays a crucial role in the overall frozen fraction of INPs. Figure 1 illustrates this effect by comparing two groups of INPs of the same size, each featuring two surface species: gray represents a highly efficient ice nucleating species ("good nucleator"), while green denotes a less effective ice nucleating species ("bad nucleator"). The group on the left represents an external mixture, where each particle consists of a single species, whereas the group on the right is an internal mixture, with both species present in each particle. During cooling, assuming the INPs are immersed in water, in case of the external mixture, only the particles that contain the good nucleator will transition to ice. In contrast, in the internal mixture, the presence of the good nucleator in all particles enables the entire population to freeze. This mechanism results in a 50% difference in ice formation, underscoring the significant impact of aerosol mixing state on ice crystal formation.

Several studies have investigated the INP mixing state impact on ice nucleation, with most focusing on changes due to chemical ageing, particularly through the coating process (Kanji et al., 2017; Knopf et al., 2018). Laboratory studies have shown that when dust particles are coated with organic material or sulfuric acid, their effectiveness as INPs is significantly reduced (Möhler et al., 2008; Sullivan et al., 2010; Kanji et al., 2017; Stevens and Dastoor, 2019). Xue et al. (2024) experimentally quantified the relative errors in contact angle measurements for sea salt particles with different mixing state during deposition ice nucleation. Their findings suggest that both the particle composition and mixing state influence the ice-nucleating abilities of marine aerosols. Similarly, Spichtinger and Cziczo (2010) used box model simulations to examine differences in deposition freezing between internally and externally mixed INPs in cirrus clouds. The study found that the contrast in freezing ability

https://doi.org/10.5194/egusphere-2025-4326
Preprint. Discussion started: 24 September 2025

between these two mixing states was more pronounced than the difference between size-dependent and size-independent nucleation threshold assumptions.

Two general approaches are commonly used to describe heterogeneous ice nucleation in atmospheric models: the singular approach (Hoose and Möhler, 2012; Niedermeier et al., 2015; Shima et al., 2020; Abade and Albuquerque, 2024) and the time-dependent approach (Fletcher, 1958, 1959, 1962; Koop et al., 2000; Knopf and Alpert, 2013; Alpert and Knopf, 2016; Knopf and Alpert, 2023), the latter based on classical nucleation theory (CNT). The singular approach assumes that each particle freezes at a characteristic temperature, independent of time, while the time-dependent formulation treats freezing as a stochastic process governed by a temperature-dependent nucleation rate. Both frameworks are simplifications of a more complex reality, and ongoing research continues to evaluate their respective merits. Notably, Arabas et al. (2025) conducted a systematic comparison and found that the CNT-based approach yields more robust results across a range of cooling conditions, particularly when laboratory-derived nucleation parameters are applied in dynamic atmospheric simulations. In this study, we adopt the CNT-based, time-dependent framework to describe immersion freezing, both for its theoretical grounding and its compatibility with our particle-resolved modeling strategy. A full implementation of both approaches is beyond the scope of this work.

While previous studies have explored the effect of mixing state on ice nucleation, significant gaps remain in understanding the specific mechanisms by which mixing state alters the INP efficiency, defined here as the fraction of particles that nucleate ice for a given temperature. Moreover, there has been a notable lack of quantitative investigations isolating the mixing state impact on freezing behavior. In many prior studies, changes in mixing state due to chemical aging or coating processes were accompanied by variations in the total surface area of different species, making it difficult to determine the direct influence of mixing state itself. To date, no particle-resolved modeling studies have been systematically quantified effect of mixing state while controlling for other factors.

To address this gap, we first develop a theoretical framework based on classical nucleation theory to quantify the sensitivity of the frozen fraction to the INPs' mixing state during the immersion freezing process. Next, we design and implement particle-resolved immersion freezing simulations within the Particle-resolved Monte Carlo Model (PartMC, Riemer et al. (2009)). This approach provides a precise and flexible representation of various mixing state, allowing us to verify our theoretical framework and quantitatively demonstrate how the frozen fraction varies as a function of INP mixing state.

2 Classical nucleation theory for mixed particles

Following classical nucleation theory, heterogeneous ice nucleation occurs when the first nucleation event on the surface of an ice nucleus triggers the entire particle to freeze. These events are stochastic Poisson processes (Pruppacher and Klett, 1979; Koop et al., 1997; Leonard and Im, 1999; Consiglio et al., 2023; Knopf and Alpert, 2023). The probability of ice nucleation within a small time step Δt assuming a constant nucleation rate λ is given by

$$P_{\text{frz}}(\Delta t) = 1 - e^{-\lambda \Delta t}, \tag{1}$$

https://doi.org/10.5194/egusphere-2025-4326
Preprint. Discussion started: 24 September 2025

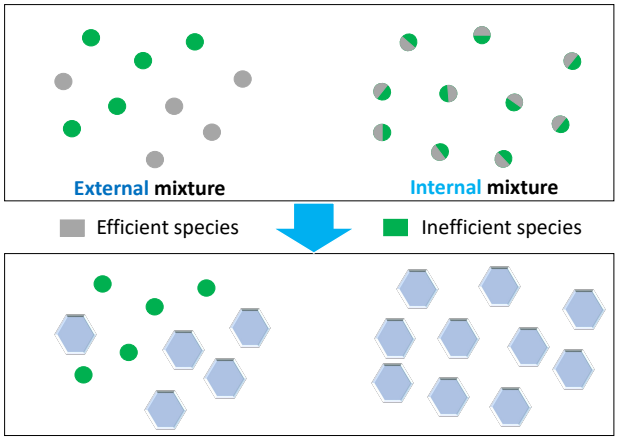

Figure 1. An example highlighting how mixing states affect the amount of ice formation. The top panel shows the INPs given at initial stage, with 50% of the INPs effective at freezing (gray) and 50% ineffective (green), distributed as both external and internal mixtures. The bottom panel displays the result after a certain duration, where the effective INPs in the internal mixture have induced a more widespread ice formation, as represented by the hexagons, compared to the external mixture.

where λ (unit: s^{-1}) depends on the size and material of the ice nucleus, as well as ambient conditions, including temperature, vapor pressure, and the properties of solutions in cases where an INP is immersed in a droplet. If λ varies over time, the probability over a period t becomes

$$P_{\text{frz}}(t) = 1 - e^{-\int_0^t \lambda(\tau) d\tau}, \tag{2}$$

as described by Koop et al. (1997); Leonard and Im (1999); Consiglio et al. (2023), and detailed in appendix A1. Since classical nucleation theory assumes that nucleation events occur randomly on the nucleus surface, λ is proportional to the surface area. This leads to the definition of the heterogeneous nucleation rate coefficient J_{het} (unit: $m^{-2}s^{-1}$), which quantifies the expected number of nucleation events per unit surface area per unit time. For an INP of surface area S_{p}, the relationship is

$$\lambda = J_{\text{het}} \cdot S_{\text{p}}. \tag{3}$$

The heterogeneous nucleation rate coefficient J_{het} depends on environmental conditions and the inherent properties of the INP. If the surface comprises regions with differing nucleation efficiencies—that is, some parts actively nucleate ice while others do not— Eq. (3) can be extended to an integral over the entire surface area:

$$\lambda = \oiint_S J_{\text{het}}(\boldsymbol{r}) \cdot dS, \tag{4}$$

where the vector $\boldsymbol{r}$ indicates a specific point on INP surface. This equation forms the foundation for simulating multi-species ice nucleation per particle. In particle-resolved models, the state of a particle is described by the amounts of its constituent species. The surface area occupied by each species can be determined with assumptions about the particle morphology. Using

https://doi.org/10.5194/egusphere-2025-4326
Preprint. Discussion started: 24 September 2025

this information, the freezing probability within Δt for a droplet containing such an INP can be expressed as

$$P_{\text{frz}}(\Delta t) = 1 - e^{-\bar{J}_{\text{het}} \cdot S_{\text{p}} \cdot \Delta t}, \tag{5}$$

where

$$\bar{J}_{\text{het}} = \frac{1}{S_{\text{p}}} \sum_{i=1}^{N_{\text{s}}} (S_i \cdot J_{\text{het}}^{(i)}) = \sum_{i=1}^{N_{\text{s}}} w_i \cdot J_{\text{het}}^{(i)}, \tag{6}$$

is the surface area weighted mean of the nucleation rate coefficient among all N_{s} species on the surface of the immersed INP, S_i is the immersed surface area covered by the i^{th} species, S_{p} is the total immersed surface area, and $w_i = S_i/S_{\text{p}}$ is the immersed surface ratio of the i^{th} species. Similarly, the freezing probability within the time range t in the Eq. (2) can be written as

$$P_{\text{frz}}(t) = 1 - e^{-S_{\text{p}} \int_0^t \bar{J}_{\text{het}}(T(\tau)) \cdot d\tau}. \tag{7}$$

For convenience, we define Φ_i, for each species as

$$\Phi_i(t) = \int_0^t J_{\text{het}}^{(i)}(T(\tau)) d\tau, \tag{8}$$

so that Eq. (7) can be simplified as

$$P_{\text{frz}}(t) = 1 - \exp\left[-S_{\text{p}} \cdot \sum_{\text{i=1}}^{N_{\text{s}}} w_i \Phi_i(t)\right]. \tag{9}$$

The value of Φ_i describes the freezing ability of the i^{th} species under a specific cooling condition. To analyze the impact of the mixing state factor on ice production, other variables affecting the amount of ice production, such as cooling rate and duration, must be controlled. Thus, under the same cooling conditions but varying mixing states, Φ_i serves as a fixed descriptor for a species' freezing capability. Additionally, Eq. (9) provides a simplified form of Eq. (7) for the theoretical analysis discussed in the following sections.

3 Sensitivity of immersion freezing to aerosol mixing state

In Section 2, Eq. (9) introduced the calculation of freezing probabilities for individual multi-species INPs. Building on this, this section examines the macroscopic frozen fraction of a multi-species INP population emphasizing the impact of mixing state on the frozen fraction. The goal is to quantify the sensitivity of the frozen fraction to aerosol mixing state during immersion freezing. The analysis focuses on monodisperse particles, with the impact on polydisperse particles left for future studies.

Even when two INP populations share the same particle count, particle sizes, and species surface area, and experience the same cooling rate, their frozen fractions can differ due to differences in mixing state. For a given scenario, we define this sensitivity as:

$$\text{Sensitivity} = \frac{f_{\text{frz}}^{(\text{max})} - f_{\text{frz}}^{(\text{min})}}{f_{\text{frz}}^{(\text{max})}} \cdot 100\%. \tag{10}$$

https://doi.org/10.5194/egusphere-2025-4326
Preprint. Discussion started: 24 September 2025

Here, $f_{\text{frz}}^{(\text{max})}$ and $f_{\text{frz}}^{(\text{min})}$ are the maximum and minimum frozen fraction values across all mixing states for the given scenario. The mixing state that produces the highest frozen fraction is referred to as the most efficient mixing state, while the one resulting in the minimum frozen fraction is termed the least efficient mixing state. The magnitude of sensitivity can also be viewed as an upper bound of the relative error in frozen fraction calculations caused by uncertainties in the mixing state.

Here, we present a theorem regarding the most and least efficient mixing states for monodisperse INPs.

Theorem 1. *For monodisperse INP populations, the internal mixture is the most efficient mixing state, while the external mixture is the least efficient mixing state.*

The proof is shown in Appendix D. Therefore, we have $f_{\text{frz}}^{(\text{max})} = f_{\text{frz}}^{(\text{int})}$, and $f_{\text{frz}}^{(\text{min})} = f_{\text{frz}}^{(\text{ext})}$, where $f_{\text{frz}}^{(\text{int})}$ and $f_{\text{frz}}^{(\text{ext})}$ are the frozen fractions corresponding to internal and external mixtures, respectively. As shown in Eq. (10), the sensitivity of monodisperse INPs depends entirely on the frozen fractions of internal and external mixture, emphasizing the need to study their differences.

It should be emphasized that Theorem 1 is only valid when internal and external mixtures of a monodisperse particle population are compared. While our framework can be applied to polydisperse populations (as discussed in Section 5.3), the distinction between internal and external mixtures is only meaningful within a single size bin—that is, mixing state comparisons are made between particles of the same size, not across different sizes.

Section 3.1 derives theoretical expressions for the frozen fraction of internal and external mixtures and offers physical insights to explain these differences. Section 3.2 examines how sensitivity is influenced by variations in species types, temperature profiles, INP sizes, and species' total surface area ratios.

3.1 Evaluating frozen fractions for internal and external mixtures

Consider an internally mixed, monodisperse INP population composed of multiple species, with N_{p} particles, each immersed in a supercooled droplet. By the Law of Large Numbers, the expected frozen fraction f_{frz} equals the arithmetic average of the freezing probabilities of all INP,

$$f_{\text{frz}} = \frac{1}{N_{\text{p}}} \sum_{j=1}^{N_{\text{p}}} P_{\text{frz},j}, \tag{11}$$

where $P_{\text{frz},j}$ is the freezing probability of the j^{th} INP as expressed in Eq. (9).

Let N_{s} denote the number of species present in the population, and $w_i = S_i/S_{\text{p}}$ represent the surface area ratio of the i^{th} species, where S_i is the area covered by species i and S_{p} is the total INP surface area.

For the externally-mixed case, the following applies. Since each particle contains only one species, the whole INP population can be conceptualized as a collection of multiple modes, with each mode representing a different species. The unfrozen fraction of the whole INP population after time t can be written

$$f_{\text{unf}}^{(\text{ext})} = \sum_{i=1}^{N_{\text{s}}} w_i \cdot f_{\text{unf}}^{(i)}, \tag{12}$$

where w_i is the ratio of the total surface area of INPs in the i^{th} mode relative to the total surface area across all INPs and $f_{\text{unf}}^{(i)}$ is the unfrozen fraction for droplets containing single-species monodisperse INPs, whose surface is 100% covered by the i^{th}

https://doi.org/10.5194/egusphere-2025-4326
Preprint. Discussion started: 24 September 2025

species (for a detailed derivation, see Appendix A2). The frozen fraction is therefore

$$f_{\mathrm{frz}}^{(\mathrm{ext})} = 1 - \sum_{i=1}^{N_\mathrm{s}} w_i \cdot f_{\mathrm{unf}}^{(i)} = 1 - \sum_{i=1}^{N_\mathrm{s}} w_i \cdot \left(1 - f_{\mathrm{frz}}^{(i)}\right), \tag{13}$$

In contrast, for the internally-mixed case the unfrozen fraction $f_{\mathrm{unf}}^{(\mathrm{int})}$ can be expressed as

$$f_{\mathrm{unf}}^{(\mathrm{int})} = \prod_{i=1}^{N_\mathrm{s}} \left[f_{\mathrm{unf}}^{(i)}\right]^{w_i}. \tag{14}$$

Thus, this leads us to an expression that captures the relationship between the frozen fraction of droplets containing multi-species INPs and single-species INPs,

$$f_{\mathrm{frz}}^{(\mathrm{int})} = 1 - \prod_{i=1}^{N_\mathrm{s}} \left(1 - f_{\mathrm{frz}}^{(i)}\right)^{w_i}, \tag{15}$$

where $f_{\mathrm{frz}}^{(\mathrm{int})}$ and $f_{\mathrm{frz}}^{(i)}$ represent the frozen fraction of droplets containing internally mixed and single-species monodisperse INPs (for detailed derivation, see Appendix A3). Eq. (14) implies that for monodisperse INPs, the internal mixture's unfrozen fraction is a weighted geometric mean of the single-species counterparts' unfrozen fractions, weighted by the species surface ratio. A mathematical description similar to Eqs. (13) and (15) is also discussed in Broadley et al. (2012).

To recap, Eqs. (13) and (15) explain the differences in ice nucleation between external and internal mixtures, which is mathematically reflected in the difference between the arithmetic and geometric means. The sensitivity of the frozen fraction to the INP mixing state becomes more pronounced when species have diverse freezing efficiencies (i.e., different $f_{\mathrm{unf}}^{(i)}$).

Despite having the same total surface area covered by a species in both the internal and the external mixture scenario, the difference in ice formation between internal and external mixtures arises because each INP freezes its droplet only once, regardless of its nucleation rate. In external mixtures (Fig. 1, left), the efficient freezing species ("good nucleator") only covers half of the INPs, so only half of the INPs are highly effective. Once these INPs freeze their droplets, any further nucleation events occurring within these already frozen droplets, though predicted by the theoretical probability model, do not lead to the formation of new ice, rendering the high efficiency of the good nucleators redundant. The remaining half consists of less effective species ("bad nucleator"), leading to fewer freezing events. In contrast, internal mixtures distribute the good nucleator across all INPs, increasing the probability of new nucleation events on unfrozen droplets and maximizing freezing efficiency.

To illustrate the results derived so far, Fig. 2 compares frozen fractions for internally-mixed and externally-mixed monodisperse INPs populations consisting of two species, species A and B. We assume that the species each cover 50% of the total INP surface area. Species A nucleates ice very efficiently with the same J_{het} as Fe_2O_3, while the J_{het} ratio of species B to A is varied (shown on the x-axis). All frozen fractions are calculated using Eqs. (9), (11), (13), and (15).

Figure 2a shows the frozen fractions for internal and external mixtures after being exposed to a constant temperature for 20 min, where the temperatures varies from -14 °C to -23 °C. As expected, the differences are more pronounced at small J_{het} ratios, where the two species' freezing efficiencies differ strongly. Concurrently, at lower temperatures, the J_{het} disparity has a larger impact, whereas at higher temperatures, the frozen fractions for both mixtures become nearly identical. Figure 2b shows

https://doi.org/10.5194/egusphere-2025-4326
Preprint. Discussion started: 24 September 2025

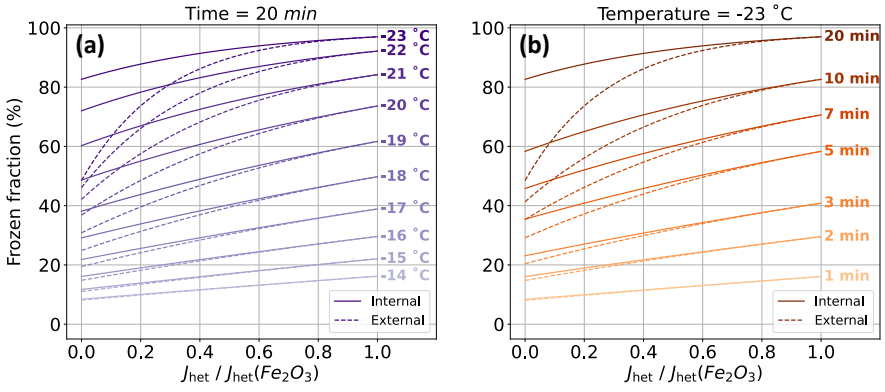

Figure 2. Frozen fractions comparing internally and externally mixed INPs after being exposed to a constant temperature for a certain time t_{freeze}. (a) Frozen fraction is evaluated for different temperatures with $t_{\mathrm{freeze}} = 20$ min. (b) Frozen fraction is evaluated for different t_{freeze} at a fixed temperature of -23 °C.

the frozen fractions over durations from 1 to 20 minutes at -23 °C. Longer durations show more pronounced differences at small J_{het} ratios, whereas shorter durations yield negligible differences. The results in both panels show a similar pattern, because lower temperatures and longer durations both lead to higher Φ values, which is the parameter that appears in Eq. (9). Since temperature and duration are combined in Φ, we will use Φ as a simpler parameter to represent freezing ability, avoiding complex cooling condition with varying temperature profiles.

3.2 Frozen fraction's sensitivity to mixing state

In the previous section, we suggested that using the Φ value simplifies the classification of cooling condition with varying temperature and duration. For example, the condition with a brief duration at low temperatures and those with longer durations at higher temperatures can be considered equivalent if they share the same Φ value. In this section, we continue using the model from Fig. 2 and analyze the effects of INP size and the total surface area fraction of each species on sensitivity of frozen fraction to mixing state.

Figure 3 introduces a sensitivity map for monodisperse INPs with dry diameter of 1 μm, and a surface ratio of two hypothetical species A and B of 50%. The x and y-axis are analogous to Fig. 2 but using Φ instead of J_{het} for the reasons stated above. Each data point in the sensitivity map represents the sensitivity value defined by Eq. (10) for a scenario involving species A and B, with typical Φ values denoted as Φ_{A} and Φ_{B}, respectively.

For reference, some atmospherically relevant examples of species combinations A and B are highlighted as horizontal dashed lines and aligned solid dots. For example, the combination of Fe_2O_3 and illite is represented by the green solid dot aligned with the gray dashed line. The Φ values for each species marked in Fig. 3 are calculated for a scenario with a constant temperature of -33 °C and a duration of 10 minutes, using Eq. (8). The J_{het} values for each species are computed using the Water Activity-Based Immersion Freezing Model (Knopf and Alpert, 2013), which is explained in more detail in Section 4.2. In Fig. 3, there

https://doi.org/10.5194/egusphere-2025-4326
Preprint. Discussion started: 24 September 2025

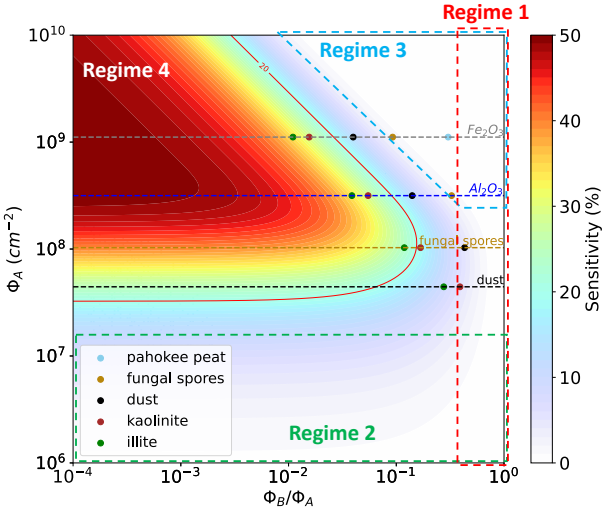

Figure 3. Sensitivity map for particles with a dry diameter of 1 μm, where species A and B are present in a 50:50 ratio. The Φ values for Fe_2O_3, Al_2O_3, fungal spores, and dust representing species A are marked by gray, blue, brown, and black horizontal dashed lines, respectively. The sky blue, brown, black, red, and green solid dots along each horizontal line represent the corresponding Φ ratios of pahokee peat, fungal spores, dust, kaolinite, and illite as species B in combination with each species A, respectively. Parameters for ice nucleation calculation are derived from Knopf and Alpert (2013).

are three regimes where uncertainties are negligible, labeled as regimes 1 to 3, and marked with red, green, and sky blue boxes, respectively.

Regime 1 represents the scenarios where two species have freezing efficiency close to each other, which results in negligible sensitivity, as discussed in Fig. 2. To explain the small sensitivities in Regimes 2 and 3, we use a simple mathematical analysis. Based on Eq. (9), the unfrozen fraction of monodisperse INPs covered by single species of A or B can be formulated as $f_{\mathrm{unf}}^{(\mathrm{A})} = \exp\left(-S_{\mathrm{p}}\Phi_{\mathrm{A}}\right)$ and $f_{\mathrm{unf}}^{(\mathrm{B})} = \exp\left(-S_{\mathrm{p}}\Phi_{\mathrm{B}}\right)$, where the $S_{\mathrm{p}} = \pi D_{\mathrm{p}}^2$ is the dry surface area of each immersed INP. Therefore, based on Eqs. (12) and (14), the unfrozen fraction of internal external mixture, denoted as $f_{\mathrm{unf}}^{(\mathrm{int})}$, can be expressed as

$$f_{\mathrm{unf}}^{(\mathrm{int})} = \exp\left[-\frac{1}{2}S_{\mathrm{p}} \cdot \left(\Phi_{\mathrm{A}} + \Phi_{\mathrm{B}}\right)\right], \tag{16}$$

while the unfrozen fraction of external mixture, denoted as $f_{\mathrm{unf}}^{(\mathrm{ext})}$, can be expressed as

$$f_{\mathrm{unf}}^{(\mathrm{ext})} = \frac{1}{2} \cdot \left[\exp\left(-S_{\mathrm{p}}\Phi_{\mathrm{A}}\right) + \exp\left(-S_{\mathrm{p}}\Phi_{\mathrm{B}}\right)\right]. \tag{17}$$

In the Regime 2, both species A and B have a relatively small Φ value of less than 10^7 cm^{-2}, where the product of S_{p} and Φ is less than the order of 10^{-1}, resulting in

$$f_{\mathrm{unf}}^{(\mathrm{int})} \approx f_{\mathrm{unf}}^{(\mathrm{ext})} \approx 1 - \frac{1}{2}S_{\mathrm{p}} \cdot \left(\Phi_{\mathrm{A}} + \Phi_{\mathrm{B}}\right), \tag{18}$$

https://doi.org/10.5194/egusphere-2025-4326
Preprint. Discussion started: 24 September 2025

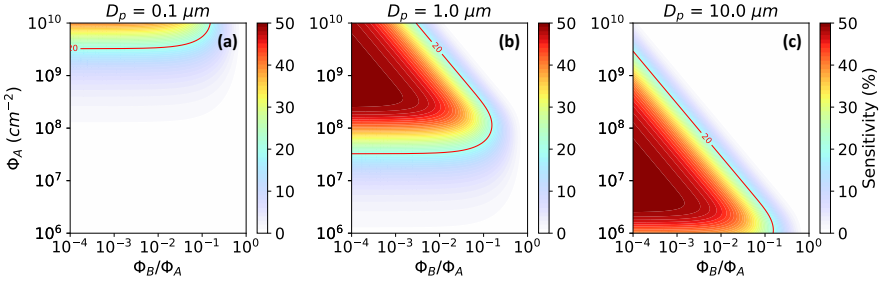

Figure 4. Same as Fig. 3 but with different dry diameter of INPs. (a): 0.1 μm; (b): 1.0 μm;(c): 10 μm.

which explains the small frozen fraction difference between internal and external mixtures in this case. This result is consistent with Fig. 2 for the conditions of higher temperature and shorter duration time.

In Regime 3, both species A and B have a large Φ value, larger than 10^8 cm^{-2}, with the product of S_p and Φ being larger than the order of 10^0, resulting in

$$f_{\text{unf}}^{(\text{int})} \approx f_{\text{unf}}^{(\text{ext})} \approx 0. \tag{19}$$

This indicates a frozen fraction of nearly 100% for both internal and external mixtures, again resulting in a small difference between the two mixing states.

Regime 4 is where the sensitivity to mixing state is significant. In this regime, the good nucleator (species A) is efficient at freezing, and a large disparity in freezing efficiency exists between the good nucleator and the bad nucleator (species B). There are several examples of species combinations that fall into Regime 4, such as Fe_2O_3 mixed with illite (34.1% of sensitivity), Fe_2O_3 mixed with kaolinite (29.0%), Al_2O_3 mixed with illite (33.7%), and dust mixed with Pahokee Peat (12.2%), among others.

Figure 4 presents the same sensitivity map as Fig. 3 but for varying INP sizes, ranging from Accumulation mode (D_p = 0.1 μm) to coarse mode (D_p = 10 μm). The pattern in the figure exhibits a vertical shift with changes in INP size: as the INP size decreases, the pattern shifts upward. In the case of smaller INPs (panels a, b), the immersed surface area of each INP is small, making it difficult for even efficient species to trigger multiple ice nucleation events on the same particle. As a result, Regime 2 dominates the entire sensitivity map. Conversely, for larger INPs with larger immersed surfaces, inefficient species can trigger multiple ice nucleation events, leading to the disappearance of Regime 2 and the dominance of Regimes 1, 3, and 4.

Figure 5 shows the same sensitivity map as Fig. 3, but for varying immersed surface ratios of species A and B. When the total immersed surface ratio of the efficient ice nucleating species (species A) is small (Figure 5a), the sensitivity increases across the entire map, especially in Regime 4, where the maximum sensitivity reaches 90%. In contrast, as the total immersed surface ratio of the efficient ice nucleating species increases, the sensitivity decreases accordingly. Once the surface ratio of species A is 90%, the maximum sensitivity is reduced to only 10%. These results indicate that when a mixed-INP population

https://doi.org/10.5194/egusphere-2025-4326
Preprint. Discussion started: 24 September 2025

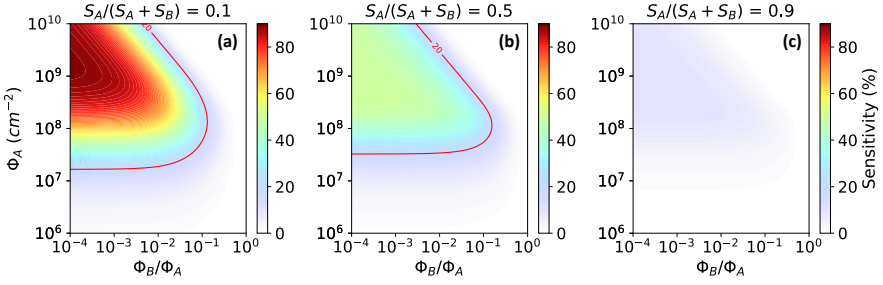

Figure 5. Same as Fig. 3 but with different total immersed surface ratio of species A (i.e., $S_A/(S_A+S_B)$). (a): 0.1; (b): 0.5; (c): 0.9.

contains a small proportion of highly efficient species, the influence of the mixing state becomes significant, and failure to accurately estimate the mixing state can lead to high error in the frozen fraction calculation.

4 Numerical implementation to particle-resolved model

Section 2 presented the immersion freezing probability for an individual mixed particle, while Section 3 analyzed the sensitivity of the frozen fraction to the mixing state of INPs. Starting from this section, we extend the theoretical framework by implementing it within the particle-resolved aerosol model (PartMC). We perform immersion freezing simulations for both single-species and multi-species INPs to confirm the results from Section 3 and further investigate the influence of INP mixing state on the frozen fraction. Section 4.1 focuses on the algorithm design for particle-resolved immersion freezing simulations, while Section 4.2 presents the simulation setup and results.

4.1 The Particle-resolved Monte-Carlo Model (PartMC)

The particle-resolved Monte Carlo (PartMC) model (Riemer et al., 2009) is a box model for simulating the evolution of aerosol particles in the atmosphere. The volume of interest contains a large quantity of discrete computational particles. Each computational particle represents a sample of real particles with identical properties (DeVille et al., 2011, 2019).

Each computational particle is assumed to be a sphere, and is represented by a vector that contains the masses of the species comprising that particle, i.e., the j^{th} particle is described as $\boldsymbol{\mu}_j = (\mu_1^j, \mu_2^j, \ldots, \mu_{N_s}^j)$, where μ_i^j is the mass of the i^{th} species in the j^{th} particle ($i \in [1, N_s]$), and N_s is the total number of species. Other characteristics of a particle such as the volume of each species, the total mass and the wet diameter (the diameter of the whole particle, including water and dissolved and insoluble aerosol material) and dry diameter (the diameter excluding water) can be derived from its mass vector.

PartMC encompasses multiple physical aerosol processes, including emission of primary aerosols, dilution with background air, coagulation (Riemer et al., 2009), and condensation of water vapor to simulate cloud formation (Ching et al., 2012). Gas-particle partitioning is included when PartMC is coupled with MOSAIC (Zaveri et al., 2008). During these processes, the evolution of the mass of each species in a particle is tracked. This feature makes PartMC a valuable tool for investigating the

https://doi.org/10.5194/egusphere-2025-4326
Preprint. Discussion started: 24 September 2025

impact of mixing state on the aerosol population and on climate-relevant properties of the aerosol. The PartMC has been used in several particle-resolved studies, e.g., Kaiser et al. (2011) used PartMC-MOSAIC to simulate the heterogeneous oxidation process on soot particles and derived the half-lives parameter of surface-bound PAHs for large-scale model. Tian et al. (2014) used it to investigate the chemical evolution of aerosols in a ship plume and its impact on CCN properties, Curtis et al. (2017) coupled PartMC-MOSAIC with WRF model to study the vertical distribution of aerosol mixing state during turbulent diffusion and dry deposition within the planetary boundary layer, Hughes et al. (2018) used the mixing state simulation result from PartMC to train the machine learning model for the global estimation of aerosol mixing state distribution, Yao et al. (2022) provided a systematic quantification of mixing state impact on aerosol optical properties based on the PartMC model simulation.

So far, PartMC has not yet been applied to questions related to heterogeneous ice nucleation. In this study, we extended PartMC by including the process of immersion freezing based on classical nucleation theory. Several parameterizations can be used to calculate the heterogeneous nucleation rate coefficient J_{het} (Fletcher, 1958, 1959, 1962; Pruppacher and Klett, 1979; Phillips et al., 2008; Hoose and Möhler, 2012; Knopf and Alpert, 2013). Following Arabas et al. (2025), we will use the activity-based immersion freezing model (ABIFM) proposed by Knopf and Alpert (2013).

4.2 The water activity-based immersion freezing model (ABIFM) for J_{het} calculation

The water activity-based immersion freezing model (ABIFM), proposed by Knopf and Alpert (2013), is a useful tool for the estimation of heterogeneous ice nucleation rate J_{het} in immersion freezing simulations. Following their study, when an INP is immersed in an aqueous solution, the rate coefficient J_{het} can be determined by the difference of solution water activity a_{w} and the water activity in equilibrium with ice $a_{\text{w}}^{\text{ice}}$. For an aerosol particle in equilibrium with ambient relative humidity, the numerical value of water activity equals the 100% of humidity (Koop et al., 2000). The parameterization of J_{het} is

$$\log_{10} J_{\text{het}} = m \cdot (a_{\text{w}} - a_{\text{w}}^{\text{ice}}) + c, \tag{20}$$

where, m and c are the ABIFM parameters for a specific aerosol species. Knopf and Alpert (2013) derived the value of m and c for ten different species fitted from experimental data, such as Fe_2O_3, Al_2O_3, fungal spores, dust, 1-Nonadecanol, kaolinite, illite, Leonardite, and Pahokee Peat.

Combining Eqs. (5), (6), and (20), the immersion freezing probability of a supercooled droplet containing one INP with multiple species can be formulated as

$$\begin{cases} P_{\text{frz}} = 1 - \exp\left[-\sum_{i=1}^{N_{\text{s}}}(w_i \cdot J_{\text{het}}^{(i)}) \cdot S_{\text{p}} \cdot \Delta t\right]; \\ \log_{10} J_{\text{het}} = m_{\text{i}} \cdot (a_{\text{w}} - a_{\text{w}}^{\text{ice}}) + c_i; \\ a_{\text{w}} = \frac{RH}{100} \approx 1;\ a_{\text{w}}^{\text{ice}} = \frac{e_{\text{s}}^{\text{ice}}(T)}{e_{\text{s}}(T)};\ w_i = \frac{S_i}{S_{\text{p}}}, \end{cases} \tag{21}$$

and the descriptions of each variable used in the Eq. (21) are listed in the Table (1).

To use Eq. (21) to calculate the immersion freezing probability of a single droplet with a multi-species insoluble INP, the immersed surface area that each species contributes must be known. However, in PartMC each particle is characterized by

https://doi.org/10.5194/egusphere-2025-4326
Preprint. Discussion started: 24 September 2025

Table 1. Parameters in Eq. (21)

Symbol	Description
$J_{\text{het}}^{(i)}$	Heterogeneous freezing rate coefficients of the i^{th} species.
S_i	Immersed surface area of i^{th} species.
S_{p}	The total immersed surface area of the INP.
Δt	Time interval.
a_{w}	Water activity of the droplet in which the INP is immersed.
$a_{\text{w}}^{\text{ice}}$	Water activity in equilibrium with ice.
RH	Relative humidity with respect to water.
e_{s}	Saturated vapor pressure with respect to water.
$e_{\text{s}}^{\text{ice}}$	Saturated vapor pressure with respect to ice.
m_i, c_i	ABIFM parameters of i^{th} species.
N_{s}	The total number of species covering the surface of the INP.

the masses of each species, and a detailed description of the particle's morphology is not tracked, and therefore appropriate assumptions need to be made. Here, we assume that the volume ratio of the species equals their surface area ratio, and that all surfaces on the insoluble INP are immersed in water.

The ice nucleation rate coefficient, $J_{\text{het}}^{(i)}$, is determined by the difference between of a_{w} and $a_{\text{w}}^{\text{ice}}$, along with the parameters m_i and c_i. Assuming the droplet remains in equilibrium with the ambient conditions and the INP it contains is insoluble, hence there is no solute present, the value of a_{w} is equal to 1. The value of $a_{\text{w}}^{\text{ice}}$ is determined by the ratio of the saturated vapor pressure with respect to ice to the saturated vapor pressure with respect to water. As temperature is the only variable that affects these terms, $a_{\text{w}}^{\text{ice}}$ is thus determined by temperature. The values of m_i and c_i for a specific species are obtained from Knopf and Alpert (2013).

4.3 The implementation to the PartMC model

This section introduces the immersion freezing simulation algorithms that we developed and implemented for the PartMC model. Simulating immersion freezing of a computational particle at a given temperature involves the following five steps (also shown in algorithm 1):

#1: Check whether the particle has an insoluble component.

#2: Assess whether the temperature is below 0 °C and if that particle is immersed in water.

#3: If a particle meets the above criteria, calculate the freezing probability P_{frz} using Eq. (21).

#4: Determine whether that particle will freeze at this time step using a stochastic method based on P_{frz}.

#5: If that particle coagulates with another frozen particle, it will also freeze.

In Step 4, if a computational particle is frozen, we assume that all real particles it represents are also frozen. Regarding Step 5, we assume that when an ice particle collides with a supercooled droplet and coalesces into a single particle, the supercooled

https://doi.org/10.5194/egusphere-2025-4326
Preprint. Discussion started: 24 September 2025

Algorithm 1 Immersion freezing algorithm for one particle

Given a particle p
if p is soluble **then**
    # The current version of PartMC does not support ice nucleation for soluble particles.
    $state\,(p) \leftarrow unfrozen$
    Return
end if
if $T > 0$ °C **then**
    $state\,(p) \leftarrow unfrozen$
    Return
end if
if p isn't immersed in water **then**
    $state\,(p) \leftarrow unfrozen$
    Return
end if
if $state\,(p) == frozen$ **then**
    $state\,(p) \leftarrow frozen$
    Return
end if
Compute freezing probability P_{frz}
if $randUnif() \leq P_{\text{frz}}$ **then**
    $state\,(p) \leftarrow frozen$
    Return
end if
if $state\,(p) == unfrozen$ **then**
    if p coagulates with a frozen particle **then**
        $state\,(p) \leftarrow frozen$
    end if
end if
Return

https://doi.org/10.5194/egusphere-2025-4326
Preprint. Discussion started: 24 September 2025

water will undergo instantaneous freezing. Algorithm 1 outlines the process for determining the freezing state of an individual particle. The function $randUnif()$ creates a random number that is uniformly distributed between 0 and 1, and the function $state(p)$ returns "frozen" or "unfrozen", showing the current phase state of particle p. To apply this in a particle-resolved model, it is equally important to develop a particle-looping algorithm that applies algorithm 1 to each particle for the entire population, which we will address next.

Denoting the complete set of particles as P, we define a subset of particles, π as a part of $P(\pi \subseteq P)$, consisting of particles that contain an insoluble core and sufficient water to satisfy the conditions necessary for immersion freezing. A straightforward algorithm to simulate immersion freezing in each time step of the PartMC model consists of iterating over all particles in π and determining the freezing state for each particle one-by-one. In this paper, we refer to this method as "Naive Algorithm" (shown in algorithm 2).

In the initial stage of PartMC simulation, the state of the particles needs to be set to "unfrozen". Then, in each time step, the PartMC model runs the algorithm 1 to update the phase state of each particle.

Algorithm 2 Naive Algorithm

1: **for** $p \in \pi$ **do**
2: Execute Algorithm 1 for p
3: **end for**

Curtis et al. (2016) proved the accuracy of this type of algorithm. However, the naive algorithm's efficiency is low when the average freezing probability P_{frz} is much less than 1. This is because it iterates through each particle, irrespective of how many actually freeze. In such scenarios, the model expends most of its time examining "unfrozen" particles one by one, only to find that the majority remains unfrozen. This process results in an inefficient use of computational resources and time.

To optimize the use of computational resources and time, we apply the Binned Tau-Leaping Algorithm (Michelotti et al., 2013; Curtis et al., 2016). This approach offers both efficiency and accuracy for stochastic particle-resolved simulations. In this approach, particles are categorized into several bins based on their size. Within each bin, the tau-leaping method is employed to enhance computational efficiency. Additionally, a secondary selection process is implemented to ensure that the algorithm accurately reflects the freezing probability associated with each particle. In this study, we have integrated the Binned Tau-Leaping Algorithm into the PartMC model to update the phase-state of particles in each timestep, detailed in algorithm 3.

We still use π to represent the set of particles that meets the prerequisite of immersion freezing. If the number of bins in PartMC is N_{bin}, define $\pi_i\,(i \in [1, N_{\text{bin}}])$ is the i^{th} bin set, and $\pi = \pi_1 \cup \pi_2 \cup \ldots \cup \pi_{N_{\text{bin}}}$, the details of the algorithm is as follow

The function $randGeom\,(P_i^{\max})$ returns a random number that follows the geometric distribution with a parameter of $P_i^{\max}$. The $|\pi_i|$ refers the number of elements in π_i. Lines 2–9 is the tau-leaping process among the particles in the i^{th} bin. $P_i^{\max}$ signifies the upper bound of the freezing probability in the i^{th} bin, a limit that the freezing probabilities of all particles within this bin should not exceed. Practically, in this algorithm, $P_i^{\max}$ is calculated by considering the largest particle in the i^{th} bin and assuming it to consist of the most efficient ice nucleation species.

https://doi.org/10.5194/egusphere-2025-4326
Preprint. Discussion started: 24 September 2025

Algorithm 3 Binned Tau-Leaping Algorithm

1: **for** $i = 1, 2, \ldots, N_{\text{bin}}$ **do**
2: compute the max probability of i^{th} bin: $P_i^{\max}$
3: $k \leftarrow |\pi_i| - 1$
4: **loop**
5: $k \leftarrow k - randGeom\,(P_i^{\max})$
6: **if** $k \leq 0$ **then**
7: break out of the loop
8: **end if**
9: select the k^{th} particle in $\pi_i : p_k^{\pi_i}$
10: **if** $state\,(p_k^{\pi_i})$ == $frozen$ **then**
11: continue loop
12: **end if**
13: compute the freezing probability of the $p_k^{\pi_i} : P_{\text{frz},k}^{\pi_i}$
14: **if** $randUnif() \leq P_{\text{frz},k}^{\pi_i} / P_i^{\max}$ **then**
15: $state\,(p_k^{\pi_i}) \leftarrow frozen$
16: **end if**
17: **end loop**
18: **end for**

Instead of checking all particles, the algorithm selects a subset of particles and bypasses the rest to enhance computational efficiency. The "jump length," which is the number of particles skipped between two selected particles, follows a geometric distribution with a parameter $P_i^{\max}$. In this sampling method, each particle in π_i has a $P_i^{\max}$ probability of being selected. Lines 13–16 detail the secondary selection process, in which each chosen unfrozen particle has a probability of $P_{\text{frz},k}^{\pi_i}$ / $P_i^{\max}$ to transition into a frozen state. After Tau-Leaping and secondary selection, the final probability for each unfrozen particles to become ice, P_k^{final}, is:

$$P_k^{\text{final}} = P_i^{\max} \cdot \frac{P_{\text{frz},k}^{\pi_i}}{P_i^{\max}} = P_{\text{frz},k}^{\pi_i} \tag{22}$$

which matches its inherent freezing probability. This attribute guarantees the precision of the Binned Tau-Leaping Algorithm, thus, at every timestep, the probability of an unfrozen particle being selected by the algorithm to change its phase state is always equal to its theoretical freezing probability as computed by the ABIFM method. A detailed proof of the algorithm's efficiency and exactness is provided by Curtis et al. (2016). Our runtime tests demonstrate that the accelerated algorithm reduces the runtime by 87.26% on average, corresponding to a 7.85× speedup, as shown in Fig. E1. The simulated frozen fractions returned by both algorithms are consistent, with RMSE less than 0.1% and $R^2 > 0.99$, as presented in Fig. E2. For details discussion on the efficiency and exactness of algorithms in PartMC run instances, please see Appendix E.

https://doi.org/10.5194/egusphere-2025-4326
Preprint. Discussion started: 24 September 2025

It is crucial to recognize that the method of grouping particles into bins and the approach used to calculate the $P_i^{\max}$ for each bin can significantly influence the algorithm's efficiency. If there is a large variance in the selection probability of particles within the same bin—meaning the upper bound value, $P_i^{\max}$, is substantially higher than the selection probabilities for the majority of particles in that bin, the algorithm's efficiency is reduced. This scenario occurs when factors other than particle size affect their selection probability. In the context of immersion freezing simulations for single-species or internally-mixed INP populations, variation in freezing probabilities are solely due to size differences, as all INPs have the same composition and are exposed to the same environmental conditions. However, for INP populations with differences in composition within a size range, $P_i^{\max}$ is calculated based on the assumption that the largest particle in the i^{th} bin is covered by the most efficient species. This can lead to a large overestimation for INPs only covered by less efficient species within that bin. A potential solution to this issue is to group INPs by both size and ice nucleation efficiency. This bin structure would ensure that $P_i^{\max}$ does not excessively exceed the probabilities of most particles in the bin, potentially enhancing the algorithm's overall efficiency. However, maintaining a two-dimensional bin structure would come with additional computational cost.

In algorithm 3, we omit the handling of the case where an unfrozen particle coagulates with a frozen particle (i.e., Lines 24–28 in algorithm 1). In the actual implementation of the PartMC model, this case is handled in the coagulation subroutine rather than in the immersion freezing subroutine.

The study in this section serves as an illustration of the application of the Binned Tau-Leaping Algorithm (Michelotti et al., 2013; Curtis et al., 2016) to accelerate particle-resolved aerosol simulations. For simulations of other physical processes that involve iteratively looping through particles and stochastically selecting some particles based on a size-related probability, the Binned Tau-Leaping Algorithm offers a promising approach for significantly reducing computational time.

5 Particle-resolved simulations of immersion freezing

This section presents the immersion freezing simulation results obtained using the PartMC model (Version 2.7.0), incorporating the algorithms developed in Section 4, alongside the theoretical results derived from the formulas described in Section 3. The objective is to illustrate variations in freezing behavior among internally and externally mixed INPs from a model simulation perspective, thereby validating the theoretical framework outlined in Section 3. Additionally, this section includes results for monodisperse INPs with intermediate mixing states, demonstrating how the frozen fraction varies with the χ index of the mixed INP population—an aspect that cannot be analytically quantified using the current theoretical framework.

5.1 Simulation settings and model assumptions

PartMC, equipped with the multi-species ABIFM algorithm, is able to simulate the changes in ice number concentration $\tilde{N}_{\text{frz}}$, and frozen fraction f_{frz} over time given a prescribed temperature profile. In this study, we conducted eight immersion freezing simulation experiments: four populations of droplets were subjected to isothermal freezing conditions, and four to a constant cooling rate freezing conditions, respectively, listed in Table (2).

https://doi.org/10.5194/egusphere-2025-4326
Preprint. Discussion started: 24 September 2025

Table 2. PartMC experiment cases

	100% illite	100% Fe_2O_3	External	Internal
constant temperature (-20 °C)	1	2	3	4
constant cooling rate (-2 °C min^{-1})	5	6	7	8

The INP populations are shown schematically in the left panel of Fig. 6. Group 1 consists solely of illite, while group 2 is exclusively made up of Fe_2O_3. In group 3, half of the particles are composed entirely of illite, and the other half entirely of Fe_2O_3, representing an external mixture. Group 4 features each particle with an even split of illite and Fe_2O_3 on its surface, constituting an internal mixture. Noting that in both the external and internal mixtures, the total surface area ratio between the two species is 50:50. All four groups of INPs share the same log-normal size distribution, with a geometric mean dry diameter of 1 μm and a log-geometric standard deviation of 0.5, shown in the right panel of Fig. 6. Specifically, for the external mixture case (Group 3), we assigned identical size distributions for Fe_2O_3 and illite particles, that is, within each size bin, the particle population comprises a 50:50 ratio of pure Fe_2O_3 to pure illite particles by number concentration. It is important to note that the population in our simulation is not monodisperse, whereas the theoretical framework presented in Section 3 is formulated for a monodisperse INP population.

The initial condition of each simulation consists of an INPs number concentration of 100 cm^{-3}. All INPs were already immersed in water (one INP per droplet) and none of the INPs was frozen. We set the initial relative humidity with respect to water at 100% to prevent evaporation of the droplets. We used 10 000 computational particles to represent the total number concentration of aerosols, with each computational particle representing 0.01 cm^{-3} aerosols sharing the same size and chemical composition.

In the isothermal experiments, the temperature was maintained at -20 °C for a duration of 10 minutes. Under the constant cooling rate freezing conditions, the temperature was reduced from -10 °C to -30 °C at a constant rate of 2 °C min^{-1} over a period of 10 minutes, i.e., $T(t) = -10\ °\mathrm{C} - 2\ °\mathrm{C\ min^{-1}} \cdot t$. The time interval Δt is set to 1 s. Within each interval from t to $t + \Delta t$, the temperature is assumed to remain constant at $T(t)$. Furthermore, the simulations were limited to immersion freezing only; emissions, dilution, and coagulation were excluded from the model.

To summarize, the assumptions in the PartMC immersion freezing simulations are: (1) All INPs are spheres, the surface area is computed by the dry diameter of INP as $S_\mathrm{p} = \pi D_\mathrm{p}^2$. (2) Each droplets contains only one INP. (3) The volume ratio of each species of mixed particles equals their surface ratio.

5.2 Simulation Results

As an example, Fig. 7 presents the results of Case 6 (all INPs consist of Fe_2O_3 and are exposed to a constant cooling rate of 2 °C min^{-1}), displaying the simulated frozen fraction and comparing it with the analytical results using Eq. (B12). As the temperature drops from -10 °C to -30 °C, more and more of INPs activate and the frozen fraction increases (green dots). The simulation results are confirmed with the analytical solution using Eq. (B12) in Appendix B.

https://doi.org/10.5194/egusphere-2025-4326
Preprint. Discussion started: 24 September 2025

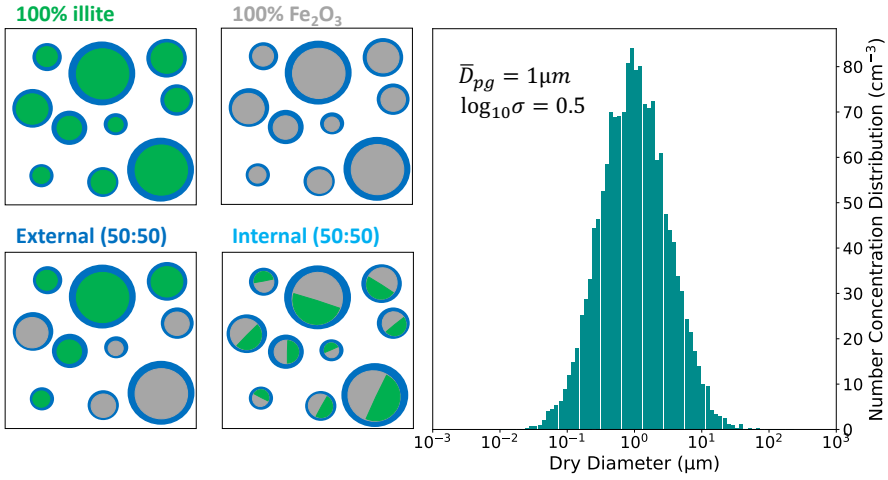

Figure 6. Model settings. Left panel: Schematic of particle mixing state for the four scenarios. The color green denotes illite, gray indicates Fe_2O_3, and blue represents the supercooled droplets that all INPs are immersed in. In both the external and internal mixtures, the total surface area ratio between the two species is 50:50. Right panel: size distribution of INPs represented by their number concentration density (cm^{-3}). The geometric mean dry diameter ($\bar{D}_{pg}$) is 1 μm and the log-geometric standard deviation ($\log_{10}\sigma$) is 0.5.

The size distributions of activated INPs at 2, 5, and 9 minutes are depicted in blue in panels (a), (b), and (c) of Fig. 7, respectively. Ice crystal formation begins in droplets containing larger INPs, which are capable of activating and freezing at higher temperatures and after shorter times. Conversely, smaller INPs require more time and lower temperatures to initiate freezing, resulting in some remaining unfrozen droplets until the end. The number concentration density function for activated INPs, analytically derived from Eq. (B10) and depicted by the black solid line in subplots (a), (b), and (c), closely aligns with the histogram representing activated INPs as predicted by the PartMC model.

Figure 8 shows the simulation results for the frozen fraction for all eight cases listed in Table (2). Panel (a) illustrated Cases 1–4 conducted at a constant temperature of $-20\,^{\circ}\mathrm{C}$, while panel (b) shows Cases 5-8, where the temperature decreased steadily from $-10\,^{\circ}\mathrm{C}$ to $-30\,^{\circ}\mathrm{C}$.

In the constant-temperature cases, the ice nucleation rate for an INP remains constant, so the frozen fraction increases over time because more time allows for more nucleation events. However, the rate of this increase slows down as fewer unfrozen droplets remain available to freeze. In scenarios with a constant cooling rate, both the frozen fraction and its rate of increase increase over time. This is because the ice nucleation rate rises as the temperature continues to drop, accelerating the freezing process.

Regardless of the temperature profile, INPs composed entirely of Fe_2O_3 consistently exhibit the highest frozen fraction. Conversely, INPs made solely of illite display the lowest frozen fraction, with internal and external mixtures of these two species falling in between.

https://doi.org/10.5194/egusphere-2025-4326
Preprint. Discussion started: 24 September 2025

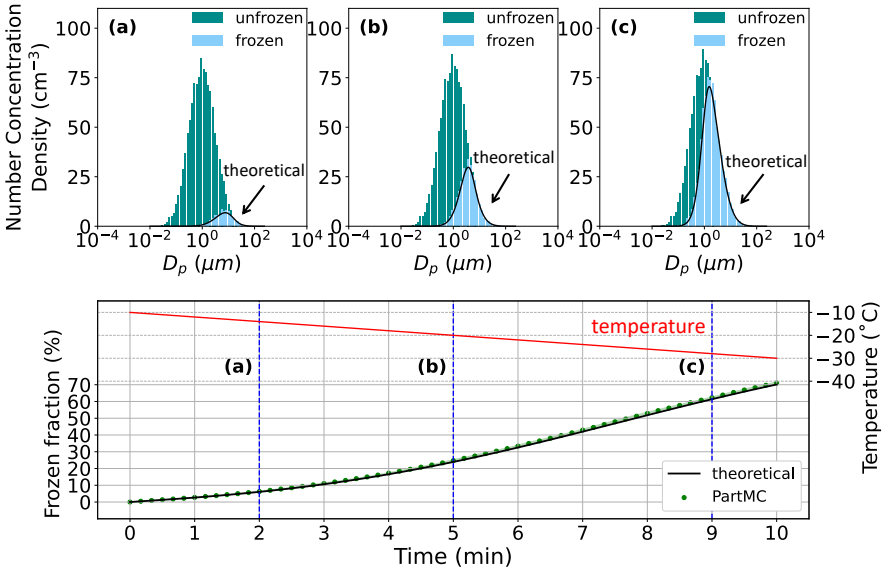

Figure 7. Comparison of model results from case 6 in Table (2) with theoretical predictions. Upper panel: Snapshots of number concentration density distribution of unfrozen (green) and frozen droplets (blue) at specific times indicated by the blue dashed lines in the lower panel. The black solid line depicts the theoretical size distribution of activated INPs calculated using Eq. (B10). Lower panel: temperature profile (red line) and time evolution of frozen fraction from 20 realizations (green dots: the average; green shading: the minimum-maximum range), and the theoretical frozen fraction calculated using Eq. (B12) (black line).

Fe_2O_3 is a highly effective freezing agent, with an ice nucleation rate coefficient of 3.5×10^4 cm^{-2}s^{-1} at -20 °C, as per the ABIFM method shown in Eq. (20). In contrast, illite exhibits a significantly lower coefficient of only 0.098 cm^{-2}s^{-1} at the same temperature. This means that Fe_2O_3's ice nucleation rate coefficient is orders of magnitude larger than that of illite. The substantial disparity in the freezing behavior of different species causes the large variations in their respective frozen fractions.

Our model results also highlight the distinctions in frozen fraction between internally and externally mixed INPs. Internally mixed INPs, comprising 50% Fe_2O_3 and 50% illite by surface area, exhibit a frozen fraction of 41% in the constant temperature scenario at the end of the simulation, and 61% in the constant cooling scenario. In contrast, externally mixed INPs, with an equal number of pure Fe_2O_3 and pure illite INPs, show a lower frozen fraction of 26% in the constant temperature simulation, and 36% in the simulation with decreasing temperature. Even though the total surface area of the INPs is the same for both species, and the cooling condition is consistent across both groups with different mixing states, a significant disparity in the frozen fraction is observed between internal and external mixtures. These results verify the main conclusion in Section 3 and underscore the importance of the mixing state as a critical factor influencing the quantity of ice formation.

Figure 9 presents another view of the comparison of frozen fraction results between analytical calculations and PartMC simulations for all eight cases listed in Table 1. Generally, the model's results closely align with the theoretical values, with an RMSE of less than 1% and a correlation coefficient exceeding 0.9999, except for Case 1. The discrepancy in Case 1 arises

https://doi.org/10.5194/egusphere-2025-4326
Preprint. Discussion started: 24 September 2025

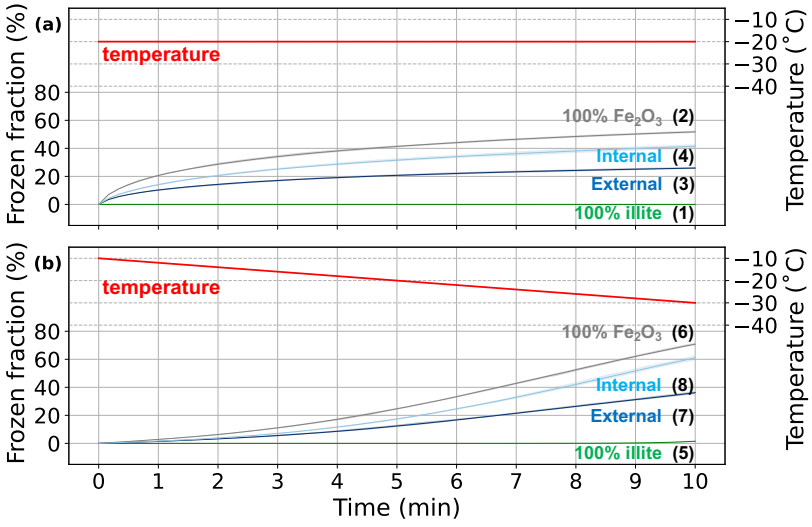

Figure 8. Simulated frozen fraction for Cases 1–8. (a) isothermal freezing conditions, Cases 1-4. (b) constant cooling rate freezing conditions, Cases 5–8. Solid lines represent the average frozen fraction from 20 repeated simulations for each scenario, and the shaded areas denote the range between the maximum and minimum values.

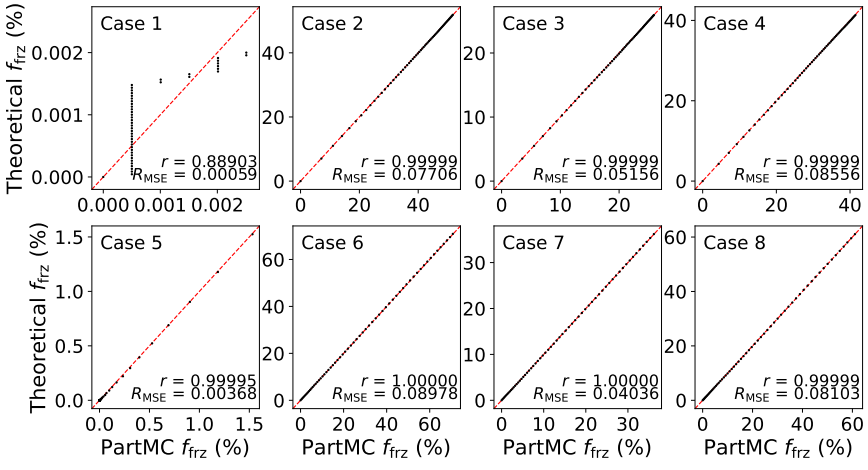

Figure 9. Simulated frozen fraction from an ensemble mean of 20 repeated PartMC simulations and analytical results for the eight cases listed in Table (2) (Cases 1–8). Each plot corresponds to one case and depicts the average frozen fraction values from the simulations against the theoretical predictions. The red dashed line represents the 1:1 line between the simulated and theoretical values.

455 from the discreteness of computational particles in the PartMC simulation. In this case, the frozen fraction is extremely low, on the order of $10^{-3}\%$, and with only 10 000 computational particles in the PartMC model, accurately predicting frozen fractions

https://doi.org/10.5194/egusphere-2025-4326
Preprint. Discussion started: 24 September 2025

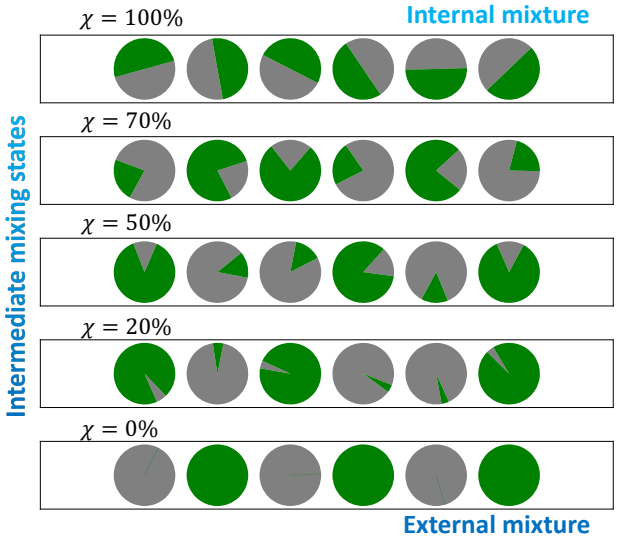

Figure 10. Schematic diagram of different aerosol mixing states described by various χ indices, where green and gray represent two different aerosol species.

below 0.01% becomes challenging. Increasing the number of computational particles could address this issue. The results in this section demonstrate the implementation of the immersion freezing algorithm for multi-species INPs in PartMC, verified against the analytical solution.

5.3 Immersion freezing simulations for INPs with intermediate mixing state

According to Theorem 1, for monodisperse particles, the frozen fractions of internally-mixed and externally-mixed INPs define the upper and lower bounds, and any intermediate mixing state will result in frozen fractions in between these two extremes. In this section, we will use PartMC to confirm this conclusion quantitatively, and discuss its applicability to polydisperse particles.

We use the χ index based on surface area as a metric to quantify the mixing state of INPs. Originally proposed by Riemer and West (2013), the χ index was designed to characterize the mixing state of an aerosol population, ranging from internally to externally mixed, based on species' mass fractions. In our study, we modify this definition by replacing mass fraction with surface area fraction for each species to better account for the ice nucleation properties of INPs (see details in Appendix F). Figure 10 illustrates the aerosol mixing states as characterized by the χ index (with respect to surface), where $\chi = 0\%$ signifies an external mixture and $\chi = 100\%$ indicates an internal mixture. Values of χ ranging between 0% and 100% denote intermediate mixtures, representing a continuum between external and internal mixing states. This conceptual framework is essential for comprehending the diverse nature of atmospheric aerosols and their varying properties.

Although Theorem 1 is formally derived for a monodisperse INP population, it can be reasonably extended to polydisperse populations, provided that the surface area ratio of species is specified within each size bin. When this condition is met, the

https://doi.org/10.5194/egusphere-2025-4326
Preprint. Discussion started: 24 September 2025

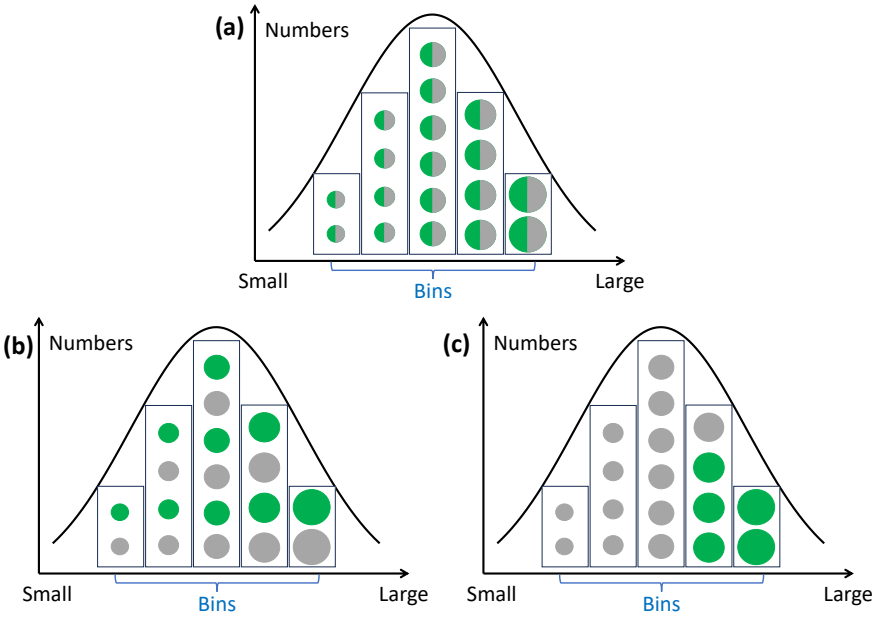

Figure 11. Schematic figure demonstrating the applicability of Theorem 1 to polydisperse INPs. Panels (a)–(c) depict the mixing states within 5-bin samples, where particles share the same size within each bin but differ in size across bins. Panel (a) represents an internal mixture, while panels (b) and (c) represent external mixtures. All three panels share the same size distribution, and the total surface area ratio between species A (gray) and B (green) is 50:50. In panels (a) and (b), the surface area ratio between species A and B is also 50:50 within each bin; however, this ratio does not hold for the INPs shown in panel (c).

polydisperse population can be treated as a collection of monodisperse subpopulations, allowing Theorem 1 to be applied to each bin individually. Under these assumptions, the internal mixture remains the most efficient one—since every particle within each bin exhibits the highest available ice nucleation efficiency—while the external mixture is the least efficient, as fewer particles possess the highly active nucleating surface. Figure 11 illustrates an applicability example of Theorem 1. The polydisperse INP populations shown in panels (a)–(c) share the same size distribution and an identical total surface area ratio of 50:50 between species A (gray) and B (green). Panel (a) shows an internal mixture, while panels (b) and (c) represent external mixtures. Theorem 1 is applicable to the efficiency comparison between panels (a) and (b), since each bin corresponding to the same INP size has the same species surface area ratio (50:50) in both cases. However, Theorem 1 is not applicable to the comparison between panels (a) and (c), because the species surface area ratio within individual bins differs. For example, while the first bin in panel (a) has a 50:50 ratio, it is 100:0 in panel (c). Similarly, other bins exhibit inconsistent ratios between panels (a) and (c), despite having the same total surface area ratio (50:50) when aggregated across all bins. Following PartMC simulation results illustrate how the frozen fraction varies with the mixing state index (χ) for a polydisperse INP population, while maintaining a 50:50 surface area ratio of Fe_2O_3 and illite particles in each bin.

https://doi.org/10.5194/egusphere-2025-4326
Preprint. Discussion started: 24 September 2025

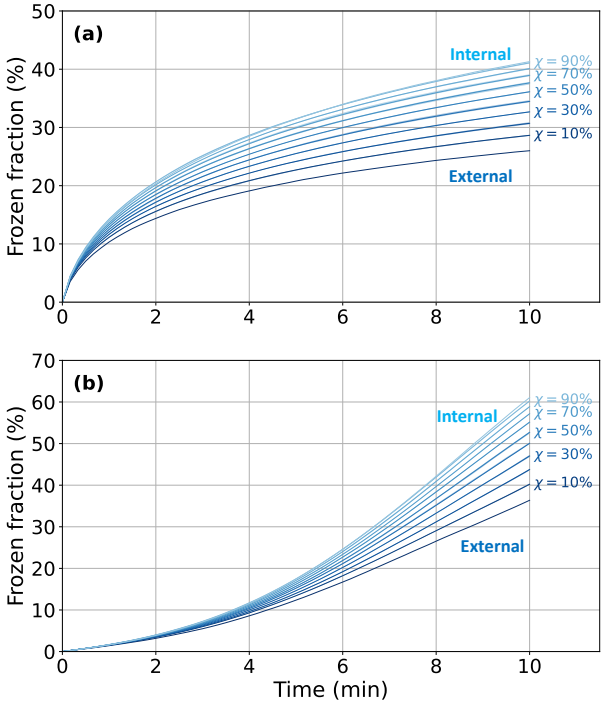

Figure 12. Time series of frozen fraction for immersed INPs with specific mixing state under a (a): isothermal freezing conditions with -20 °C and (b): constant cooling rate freezing conditions from -10 °C to -30 °C within 10 minutes. Each line corresponds to a specific mixing state of INPs, identified by varying values of the mixing state index χ, which ranges from 0% (purely external mixture) to 100% (purely internal mixture).

We initialized the model with a series of INP populations characterized by varying intermediate mixing states, with the χ value for INPs in each bin were set to 10%, 20%, 30%, 40%, 50%, 60%, 70%, 80%, and 90% for each respective simulation case respectively. All populations shared the same size distribution, as illustrated in the right panel of Fig. 6, and had a same number concentration of 100 cm^{-3}. Each INP population was divided into 100 size bins, within which the total surface ratio is composed of 50% Fe_2O_3 and 50% illite. The method we used to construct an intermediate mixing states with a specific χ in each bin is detailed in Appendix G.

Two types of simulation were conducted for each of the nine INP populations with intermediate mixing states. One is the isothermal scenario, with a constant temperature of -20 °C for 10 minutes, the same as Cases 1–4; the other involves a constant cooling rate of -2 °C min^{-1} over 10 minutes, the same as Cases 5–8. All model assumptions are the same as those in Section 5.1, so that the isothermal simulations for intermediate mixing state INPs are comparable to Cases 3 (external mixture) and 4 (internal mixture), and constant cooling rate simulations are comparable to Cases 7 (external mixture) and 8 (internal mixture).

https://doi.org/10.5194/egusphere-2025-4326
Preprint. Discussion started: 24 September 2025

The time series of simulated frozen fraction for all intermediate mixing state cases are shown in Fig. 12, with the upper panel representing the isothermal experiments and the lower panel representing the constant cooling experiments. Cases 3 and 4 are also shown in the upper panel as references for external and internal mixtures in the constant temperature scenario, marked as χ=0% and χ=100%, respectively. Similarly, results from Cases 7 and 8 are shown in the lower panel as references for external and internal mixtures in the constant cooling scenario. Regardless of whether the scenario involves constant temperature or constant cooling rate, the frozen fractions of intermediate-mixed INPs fall between those of internally and externally mixed INPs, ordered according to the χ value.

The frozen fractions of the internal and external mixtures set the upper and lower bounds for the frozen fraction of the intermediate mixing state, respectively. This confirms the argument made in Theorem 1. In cases where the mixing state is unknown, assuming the INP population is in an internal mixture during simulations would lead to the largest error in the frozen fraction estimation if the actual state is an external mixture. All other intermediate mixing states would result in smaller errors. The uncertainty mentioned here can be quantified by the sensitivity defined by Eq. (10), which describes the maximum range of the "mixing state effect" on the frozen fraction.

6 Discussion and Conclusion

This study developed a theoretical and modeling framework to quantify how aerosol mixing state influences immersion freezing. We derived analytical expressions linking the frozen fraction to particle composition and mixing state, showing that internally mixed populations yield systematically higher ice fractions than externally mixed ones under identical environmental conditions.

We implemented a multi-species immersion freezing scheme in the particle-resolved model PartMC, using the ABIFM parameterization for heterogeneous nucleation rates. To improve computational efficiency, we incorporated a Binned Tau-Leaping algorithm, which achieved nearly an order-of-magnitude speedup while preserving accuracy. Simulations validated the theoretical results and quantified the influence of particle size, species type, and surface coverage on freezing behavior.

It is important to note that this study exclusively adopts the time-dependent description of immersion freezing based on classical nucleation theory (CNT). While there is ongoing debate in the community regarding the relative merits of the CNT-based (stochastic) and singular (threshold-based) approaches, we focus here on CNT to avoid additional complexity and to build on a physical framework. Recent comparative evaluations, both in context of laboratory studies (e.g., Szakáll et al., 2021) and model development (e.g., Arabas et al., 2025), suggest that CNT offers greater robustness, also in light of capturing multiple-component aerosol materials. Nevertheless, we acknowledge that neither approach may fully capture the true nature of atmospheric ice nucleation, and future work could explore extensions of this framework to include singular formulations.

The PartMC model calculates the surface area of INPs based on their dry diameter, assuming that the particles are spherical. However, real atmospheric aerosols exhibit a wide range of shapes and surface textures (e.g., Dick et al., 1998; Chou et al., 2008; Adachi et al., 2010; Valsan et al., 2016; Conny and Buseck, 2024), which challenges the validity of this simplifying assumption. Even particles that appear approximately spherical may have complex surface features—such as folds, pits, or

https://doi.org/10.5194/egusphere-2025-4326
Preprint. Discussion started: 24 September 2025

protrusions—that lead to underestimation of their true surface area when diameter alone is used. Accurately representing the ice-nucleating potential of such particles in atmospheric models therefore requires a more realistic estimation of surface area (Alpert and Knopf, 2016; Knopf et al., 2020). One approach is to compute a surface-area-equivalent diameter, which can then be used as model input to reduce biases in ice nucleation predictions arising from the spherical assumption.

The current algorithm is designed to simulate immersion freezing in particles composed entirely of insoluble species, such as illite, kaolinite, Fe_2O_3, and Al_2O_3. Its applicability becomes limited, however, when particles contain soluble components, requiring a more nuanced treatment. If a particle is fully soluble, it dissolves completely upon droplet formation, leaving no solid surface to initiate immersion freezing. In such cases, only homogeneous nucleation is expected. For mixed particles containing both soluble and insoluble components, the soluble fraction dissolves into the droplet, altering its water activity a_w, which then deviates from that of pure water ($a_w = 1$; see Eq. (20)). This shift must be quantified based on the ratio of soluble material to water volume (Berkemeier et al., 2016; Charnawskas et al., 2017; Knopf et al., 2018). The remaining insoluble core can still act as an INP, but its surface area may differ significantly from that of the original particle, requiring recalculation based on the volume of the insoluble fraction. Additionally, certain species—such as 1-nonadecanol—can act as surfactants, forming films on the droplet surface and increasing the effective ice-nucleating area. To account for these complexities, the model will need to be expanded in future work to include the effects of solubility, water activity, and surfactant behavior on ice nucleation.

The theoretical investigation revealed that the fundamental difference in the unfrozen fraction between internally and externally mixed INPs is mathematically equivalent to the difference between the surface area-weighted geometric and arithmetic means of the frozen fractions that each species would exhibit if it individually dominated the INPs. Under identical environmental conditions, internally mixed monodisperse INP populations exhibit the highest frozen fraction, whereas externally mixed populations exhibit the lowest, with all other intermediate mixing states falling within this range. A systematic analysis of the sensitivity map reveals that in INP populations composed of multiple species, the impact of the mixing state becomes significant when there is a species with very high freezing efficiency that differs markedly from the other species, especially when this species occupies only a small fraction of the total surface area. These insights highlight the profound impact of the mixing state on ice formation processes, particularly when INPs comprise materials with notably diverse freezing characteristics. This research emphasizes the importance of considering the mixing state of INPs to enhance the precision of ice nucleation predictions in mixed-phase cloud environments.

The particle-resolved simulation results of immersion freezing using the PartMC model demonstrated a robust representation of the immersion freezing process, well-supported by theoretical predictions. Further analysis highlighted the superiority of the Binned Tau-leaping algorithm over the naive algorithm, both in terms of efficiency and precision, for predicting INPs' freezing behavior. The simulated frozen fraction results showed excellent agreement with theoretical calculations, providing successful verification of the frozen fraction equation proposed in this study. Significant distinctions were observed in PartMC simulations between single-species and multi-species INPs, as well as between INPs in internal and external mixtures. Simulations of intermediate mixed INPs confirmed that, for monodisperse INP populations (or INPs within the same bin), internal and external mixtures represent two extreme cases that define the upper and lower bounds for other mixing states. This finding is consistent

https://doi.org/10.5194/egusphere-2025-4326
Preprint. Discussion started: 24 September 2025

with the theoretical conclusions presented earlier. Furthermore, the results quantitatively demonstrated that the frozen fraction increases with the χ index of two-species INPs, providing a illustration of how the mixing state influences the frozen fraction of mixed INPs.

With the advancement of single-particle analytical techniques capable of identifying surface chemical composition (e.g., Knopf et al., 2014; Laskin et al., 2016; Knopf et al., 2018, 2021; Lata et al., 2021; Alpert et al., 2022; Knopf et al., 2023; Xue et al., 2024), the model developed here is well suited to incorporate such detailed particle-level information, enabling more accurate predictions of immersion freezing and, ultimately, improved estimates of ice crystal number concentrations.

Code and data availability. The data used to reproduce the figures are available at https://doi.org/10.13012/B2IDB-6849781_V1 (Tang et al., 2025). The PartMC v2.8.0, modified to include immersion freezing, is available at https://github.com/tangwhiap/partmc/tree/imf (West et al., 2025). PyPartMC v2.0.0 is archived at https://zenodo.org/records/17113809 (D'Aquino et al., 2024), where the Jupyter notebook for reproducing numerical simulations and figures in section 5 is provided at `examples/immersion_freezing.ipynb`.

Appendix A: Derivation details

A1 Derivation of the single-particle freezing probability: equation (2)

The immersion freezing probability of supercooled droplet can be decreased by the Poisson model (Pruppacher and Klett, 1979; Koop et al., 1997), the probability of N ice nucleation triggering events occurring within time Δt is

$$P(N, \Delta t) = \frac{1}{N!} \cdot (\lambda t)^N \cdot e^{-\lambda \Delta t}, \tag{A1}$$

where λ represents the ice nucleation rate (unit: s^{-1}). Therefore, the probability of $N \geq 1$ events occuring during Δt is

$$P_{\text{frz}}(\Delta t) = P(N \geq 1, \Delta t) = 1 - P(N = 0, \Delta t) = 1 - e^{-\lambda \Delta t}, \tag{A2}$$

which is also the freezing probability of a particle within the time interval Δt, shown in Eq. (1).

Let us divide the total cooling time, denoted as t, into h discrete time intervals Δt. Thus, we have

$$t = h \cdot \Delta t. \tag{A3}$$

If a droplet remains unfrozen until the time t, it was unfrozen throughout each time interval. On the other hand, if it freezes at any time point, it will remain frozen for the remainder of the simulation, as the melting process is not considered. Here, we regard the ice nucleation rate as a function of time, denoted by $\lambda(\tau)$, and the probability of a droplet remaining unfrozen from t_1 to t_2 is denoted by $P_{\text{unf}}(t_1, t_2)$. The probability of a droplet remaining unfrozen from 0 to t, denoted by $P_{\text{unf}}(0, t)$, can be

https://doi.org/10.5194/egusphere-2025-4326
Preprint. Discussion started: 24 September 2025

formulated as

$$P_{\text{unf}}(0,t) = P_{\text{unf}}(0,\Delta t)\cdot P_{\text{unf}}(\Delta t,2\Delta t)\cdot P_{\text{unf}}(2\Delta t,3\Delta t)\cdot \ldots \cdot P_{\text{unf}}((h-1)\Delta t,h\Delta t) \tag{A4}$$

$$= \exp\left[-\lambda(0)\cdot\Delta t\right]\cdot\exp\left[-\lambda(\Delta t)\cdot\Delta t\right]\cdot\exp\left[-\lambda(2\Delta t)\cdot\Delta t\right]\cdot \tag{A5}$$

$$\ldots\cdot\exp\left[\lambda((h-1)\Delta t)\cdot\Delta t\right] = e^{-\left[\sum_{k=0}^{h-1}\lambda(k\Delta t)\cdot\Delta t\right]}. \tag{A6}$$

Considering the limits $\Delta t \to 0$ and $h \to \infty$, the unfrozen probability $P_{\text{unf}}(0,t)$ will involve the time integration of λ:

$$P_{\text{unf}}(0,t) = \lim_{\Delta t\to 0, h\to+\infty} e^{-\left[\sum_{k=0}^{h-1}\lambda(k\Delta t)\Delta t\right]} = e^{-\int_0^t \lambda(\tau)d\tau}. \tag{A7}$$

Therefore, the probability of freezing from $t=0$ to t is

$$P_{\text{frz}}(0,t) = 1 - e^{-\int_0^t \lambda(\tau)d\tau}, \tag{A8}$$

where $P_{\text{frz}}(0,t)$ is, for simplicity, denoted as $P_{\text{frz}}(t)$ in Eq. (2).

A2 Derivation of the frozen fraction equation for monodisperse INPs with external mixture: equation (13)

An externally mixed monodisperse INP population can be conceptualized as a collection of multiple modes, with each mode representing particles composed of a single species. Let us define w_i as the ratio of the total surface area covered by the i^{th} species relative to the total surface area across all INPs

$$w_i = \frac{\sum_{j=1}^{N_{\text{p}}} S_j^{(i)}}{\sum_{j=1}^{N_{\text{p}}} S_{\text{p}_j}}, \tag{A9}$$

where, S_{p_j} is the immersed surface area of the j^{th} particle, and $S_j^{(i)}$ denotes the area covered by the i^{th} species on the j^{th} particle. For a monodisperse INP population, all INPs are assumed to have the same immersed surface area, $S_{\text{p}_j} = S_{\text{p}}$. As each INP is covered by a single species, these ratios are determined purely by the numbers of INPs within each mode. Thus, the total surface area ratio of i^{th} species equals the fraction of INPs that covered by the i^{th} species:

$$w_i = \frac{\sum_{j=1}^{N_{\text{p}}} S_j^{(i)}}{\sum_{j=1}^{N_{\text{p}}} S_{\text{p}_j}} = \frac{N_{\text{p}}^{(i)} S_{\text{p}}}{N_{\text{p}} S_{\text{p}}} = \frac{N_{\text{p}}^{(i)}}{N_{\text{p}}} \tag{A10}$$

where $N_{\text{p}}^{(i)}$ is the total number of the i^{th} mode particle. The overall number of unfrozen particles is the sum of the number of unfrozen particles from all modes

$$N_{\text{unf}} = \sum_{i=1}^{N_{\text{s}}} N_{\text{unf}}^{(i)}, \tag{A11}$$

where $N_{\text{unf}}^{(i)}$ is the number of unfrozen particles for the mode consisting of INPs covered by the i^{th} species. Following the definition of unfrozen fraction, and incorporating Eqs. (A10) and (A11), the unfrozen fraction is given by

$$f_{\text{unf}}^{(\text{ext})} = \frac{N_{\text{unf}}}{N_{\text{p}}} = \frac{1}{N_{\text{p}}}\cdot\sum_{i=1}^{N_{\text{s}}} N_{\text{unf}}^{(i)} = \frac{1}{N_{\text{p}}}\cdot\sum_{i=1}^{N_{\text{s}}} N_{\text{p}}^{(i)}\cdot f_{\text{unf}}^{(i)} = \sum_{i=1}^{N_{\text{s}}} w_i\cdot f_{\text{unf}}^{(i)}, \tag{A12}$$

https://doi.org/10.5194/egusphere-2025-4326
Preprint. Discussion started: 24 September 2025

where $f_{\text{unf}}^{(i)}$ denotes the unfrozen fraction of INPs in the i^{th} mode. The Eq. (A12) is the same as Eq. (12) in the Section 3.1. Since $f_{\text{frz}}^{(\text{ext})} = 1 - f_{\text{unf}}^{(\text{ext})}$ and $f_{\text{frz}}^{(i)} = 1 - f_{\text{unf}}^{(i)}$, there is

$$f_{\text{frz}}^{(\text{ext})} = 1 - \sum_{i=1}^{N_\text{s}} w_i \cdot f_{\text{unf}}^{(i)} = 1 - \sum_{i=1}^{N_\text{s}} w_i \cdot \left(1 - f_{\text{frz}}^{(i)}\right), \tag{A13}$$

which is the Eq. (13) shown in Section 3.1.

A3 Derivation of the frozen fraction equation for monodisperse INPs with internal mixture: equation (15)

For an INP immersed in a supercooled droplet, composed of multiple species, let the total number of species be N_s, with $w_i = S_i/S$ denoting the surface covering ratio of the i^{th} species, where S_i is the area covered by the i^{th} species and S is the total surface area of the INP. Assuming the temperature remains below 0 °C, based on Eq. (9), the probability of the droplet remaining unfrozen after time t is

$$P_{\text{unf}}(t) = 1 - P_{\text{frz}}(t) = e^{-S_\text{p} \cdot \sum_{i=1}^{N_\text{s}} w_i \Phi_i(t)}. \tag{A14}$$

Denoting $P_{\text{unf}}^{(i)} = e^{-S_\text{p} \cdot \Phi_i(t)}$ the droplet's unfrozen probability for an INP of the same size but with its surface 100% covered by the i^{th} species, we obtain

$$P_{\text{unf}}^{(i)} = 1 - P_{\text{frz}}^{(i)} = e^{-S_\text{p} \cdot \Phi_i(t)}, \forall i \in [1, N_\text{s}]. \tag{A15}$$

Combining Eq. (A14) and Eq. (A15) gives:

$$P_{\text{unf}} = 1 - P_{\text{frz}} = e^{-S_\text{p} \cdot \sum_{i=1}^{N_\text{s}} w_i \cdot \Phi_i(t)} = \prod_{i=1}^{N_\text{s}} \left[e^{-S_\text{p} \cdot \Phi_i(t)}\right]^{w_i} = \prod_{i=1}^{N_\text{s}} \left[P_{\text{unf}}^{(i)}\right]^{w_i}. \tag{A16}$$

For an internally mixed population of monodisperse INPs, each INP has the same size and the ratio of surface covered by each species. Therefore, the freezing probabilities are the same for each INP (same for the unfrozen probabilities). Based on the Law of Large Numbers, the unfrozen fraction equals the unfrozen probability of each droplet,

$$f_{\text{unf}} = P_{\text{unf}}. \tag{A17}$$

The same also applies for monodisperse INPs covered by a single species i:

$$f_{\text{unf}}^{(i)} = P_{\text{unf}}^{(i)}, \forall i \in [1, N_\text{s}]. \tag{A18}$$

Substituting Eqs. (A17) and (A18) to Eq. (A16), we have:

$$f_{\text{unf}}^{(\text{int})} = \prod_{i=1}^{N_\text{s}} \left[f_{\text{unf}}^{(i)}\right]^{w_i}, \tag{A19}$$

the same as Eq. (14) in Section 3.1. Since $f_{\text{frz}}^{(\text{int})} = 1 - f_{\text{unf}}^{(\text{int})}$ and $f_{\text{frz}}^{(i)} = 1 - f_{\text{unf}}^{(i)}$, there is

$$f_{\text{frz}}^{(\text{int})} = 1 - \prod_{i=1}^{N_\text{s}} \left[1 - f_{\text{frz}}^{(i)}\right]^{w_i}, \tag{A20}$$

which is equal to Eq. (15) shown in Section 3.1.

https://doi.org/10.5194/egusphere-2025-4326
Preprint. Discussion started: 24 September 2025

Appendix B: Ice number concentration for single-mode polydisperse INP population

Equation (9) outlines the freezing probability for an individual droplet. In this appendix, we derive equations that describe the ice crystal number concentration and the frozen fraction for a collection of single-mode INPs immersed in supercooled droplets, subject to a specific temperature profile. A "mode" in this context refers to a group of particles whose sizes follow a specified distribution, and all particles within the mode have the same composition.

Assuming that each droplet contains only one INP, and each INP is spherical. The surface area of each INP, S_p, can be calculated by

$$S_\mathrm{p} = \pi D_\mathrm{p}^2. \tag{B1}$$

It is also assumed that no ice formation occurs at the initial time. Additionally, we maintain the temperature below 0 °C throughout the simulation to prevent melting. Moreover, we assume that all INPs contain the same species types and their surface coverage for all INPs is identical (i.e., single-species and internally mixed INPs with respect to surface), in order to satisfy the definition of the single-mode particles.

For monodisperse INPs, given that the size and surface fractions of species are uniform across all INPs, all droplets have the same freezing probability at any given time. According to the Law of Large Numbers, the expected value of the frozen fraction is equivalent to the freezing probability of each individual droplet

$$f_\mathrm{frz}(t) \equiv P_\mathrm{frz}(t). \tag{B2}$$

Consequently, the ice number concentration can be expressed as

$$\tilde{N}_\mathrm{frz}(t) = \tilde{N}_\mathrm{t} \cdot f_\mathrm{frz}(t) = \tilde{N}_\mathrm{t} \cdot P_\mathrm{frz}(t). \tag{B3}$$

In the case of polydisperse INPs, the freezing probability of each droplet varies depending on the diameter of the contained INP, denoted as $P_\mathrm{frz}(t, D_\mathrm{p})$. Combining Eq. (9) and Eq. (B1), we have

$$P_\mathrm{frz}(t,\ D_\mathrm{p}) = 1 - e^{-\pi D_\mathrm{p}^2 \cdot \bar{\Phi}(t)}. \tag{B4}$$

where $\bar{\Phi}(t)$ represents the time integrated surface area-weighted mean of the ice nucleation rate coefficient, given by

$$\begin{aligned}\bar{\Phi}(t) &= \int_0^t \bar{J}_\mathrm{het}(T(\tau))d\tau = \int_0^t \sum_{i=1}^{N_\mathrm{s}} w_i \cdot J_\mathrm{het}^{(i)}(T(\tau))d\tau \\ &= \sum_{i=1}^{N_\mathrm{s}} w_i \cdot \left(\int_0^t J_\mathrm{het}^{(i)}(T(\tau))d\tau\right) = \sum_{i=1}^{N_\mathrm{s}} w_i \cdot \Phi_i(t),\end{aligned} \tag{B5}$$

Herein, we define the size distribution density function $n_\mathrm{N}(\ln D_\mathrm{p})$ to represent the size distribution of INPs. Analogous to the Eq. (B3), the size distribution density function for "activated" INPs (those that cause the freezing of droplet in which they are immersed) can be expressed as

$$n_\mathrm{frz}(t,\ \ln D_\mathrm{p}) = n_\mathrm{N}(\ln D_\mathrm{p}) \cdot P_\mathrm{frz}(t,\ D_\mathrm{p}) = n_\mathrm{N}(\ln D_\mathrm{p}) \cdot (1 - e^{-\pi D_\mathrm{p}^2 \cdot \bar{\Phi}(t)}). \tag{B6}$$

https://doi.org/10.5194/egusphere-2025-4326
Preprint. Discussion started: 24 September 2025

Consequently, the ice crystal number concentration, which is the aggregate of the numbers of "activated" INPs across all sizes, can be calculated as follows

$$\tilde{N}_{\mathrm{frz}}(t) = \int_{-\infty}^{+\infty} n_{\mathrm{frz}}(t,\ \ln D_{\mathrm{p}}) \cdot dlnD_{\mathrm{p}} = \tilde{N}_{\mathrm{t}} - \int_{-\infty}^{+\infty} n_{\mathrm{N}}(t,\ \ln D_{\mathrm{p}}) \cdot e^{-\pi D_{\mathrm{p}}^2 \cdot \bar{\Phi}(t)} d\ln D_{\mathrm{p}}, \tag{B7}$$

and the frozen fraction can be derived by

$$f_{\mathrm{frz}} = \tilde{N}_{\mathrm{frz}}(t)/\tilde{N}_{\mathrm{t}} = 1 - \frac{1}{\tilde{N}_{\mathrm{t}}} \cdot \int_{-\infty}^{+\infty} n_{\mathrm{N}}(t,\ \ln D_{\mathrm{p}}) \cdot e^{-\pi D_{\mathrm{p}}^2 \cdot \bar{\Phi}(t)} d\ln D_{\mathrm{p}}. \tag{B8}$$

In the PartMC simulations mentioned in section 5, the INPs are assumed to be log-normally distributed, with a specific geometric mean diameter $\bar{D}_{\mathrm{pg}}$, geometric standard deviation σ_{g}, and a total number concentration $\tilde{N}_{\mathrm{t}}$. The size distribution density function is given by:

$$n_{\mathrm{N}}(\ln D_{\mathrm{p}}) = \frac{\tilde{N}_{\mathrm{t}}}{\sqrt{2\pi} \cdot \ln \sigma_{\mathrm{g}}} e^{-\frac{(\ln D_{\mathrm{p}} - \ln \bar{D}_{\mathrm{pg}})^2}{2\ln^2 \sigma_{\mathrm{g}}}}. \tag{B9}$$

Upon substituting Eq. (B9) to the Eq. (B6), the resultant size distribution density function for the activated INPs is

$$n_{\mathrm{frz}}(t,\ \ln D_{\mathrm{p}}) = \frac{\tilde{N}_{\mathrm{t}}}{\sqrt{2\pi} \cdot \ln \sigma_{\mathrm{g}}} e^{-\frac{(\ln D_{\mathrm{p}} - \ln \bar{D}_{\mathrm{pg}})^2}{2\ln^2 \sigma_{\mathrm{g}}}} \cdot (1 - e^{-\pi D_{\mathrm{p}}^2 \cdot \bar{\Phi}(t)}). \tag{B10}$$

Similarly, by inserting Eq. (B9) into Eq. (B7), we derive the expression for the ice crystal number concentration as

$$\tilde{N}_{\mathrm{frz}}(t) = \tilde{N}_{\mathrm{t}} - \frac{\tilde{N}_{\mathrm{t}}}{\sqrt{2\pi} \cdot \ln \sigma_{\mathrm{g}}} \cdot \int_{-\infty}^{+\infty} \exp\left[-\frac{(\ln D_{\mathrm{p}} - \ln \bar{D}_{\mathrm{pg}})^2}{2\ln^2 \sigma_{\mathrm{g}}} - \pi D_{\mathrm{p}}^2 \cdot \bar{\Phi}(t) \right] d\ln D_{\mathrm{p}}. \tag{B11}$$

Further, by applying Eq. (B9) to Eq. (B8), the expression for the frozen fraction is established as

$$f_{\mathrm{frz}}(t) = 1 - \frac{1}{\sqrt{2\pi} \cdot \ln \sigma_{\mathrm{g}}} \cdot \int_{-\infty}^{+\infty} \exp\left[-\frac{(\ln D_{\mathrm{p}} - \ln \bar{D}_{\mathrm{pg}})^2}{2\ln^2 \sigma_{\mathrm{g}}} - \pi D_{\mathrm{p}}^2 \cdot \bar{\Phi}(t) \right] d\ln D_{\mathrm{p}}. \tag{B12}$$

Equations (B11),(B12), combined with Eqs. (B5) and (20), relate the metrics of immersion freezing to the INP size distribution parameters, the chemical composition of INPs, and the temperature profile, which are input parameters for PartMC. The ice crystal number concentrations and frozen fractions, as determined by Eqs. (B11) and (B12), are thus analytical solutions for scenarios where the INP population contains either a single species or multiple species in an internal mixture.

Equations (B11),(B12) provide the framework for verifying the expected ice crystal number concentration and frozen fraction for all simulations conducted in Section 5.1 (shown in Table 2), except Cases 3 and 7 (because these involve two modes of INPs). The cases differ in the species combinations and temperature profiles. For instance, in Case 1, where the temperature remains constant at $-20\ ^{\circ}\mathrm{C}$ and the INPs consist solely of illite, the $\bar{\Phi}$ in Eqs. (B11) and (B12) is

$$\bar{\Phi}(t) = \Phi_{\mathrm{illite}}(t) = J_{\mathrm{het}}^{\mathrm{illite}}(-20\ ^{\circ}\mathrm{C}) \cdot t. \tag{B13}$$

In Case 6, a linear temperature decrease ($2\ \mathrm{K\,min^{-1}}$) is applied and only Fe_2O_3, $\bar{\Phi}$ is present. Therefore $\bar{\Phi}$ is

$$\bar{\Phi}(t) = \Phi_{\mathrm{Fe_2O_3}}(t) = \int_0^t J_{\mathrm{het}}^{\mathrm{Fe_2O_3}}(T(\tau)) d\tau, \tag{B14}$$

https://doi.org/10.5194/egusphere-2025-4326
Preprint. Discussion started: 24 September 2025

where, $T(\tau)$ follows is the linear temperature profile. Similarly, for Case 8, which involves an internal mixture of 50% illite and 50% Fe_2O_3, $\bar{\Phi}$ is

$$\bar{\Phi}(t) = \frac{1}{2}(\Phi_{\text{illite}} + \Phi_{\text{Fe}_2\text{O}_3}) = \frac{1}{2}\int_0^t J_{\text{het}}^{\text{illite}}(T(\tau)) + J_{\text{het}}^{\text{Fe}_2\text{O}_3}(T(\tau))d\tau. \tag{B15}$$

The expressions for calculating the ice crystal number concentration and frozen fraction in external mixture scenarios, particularly pertaining to Cases 3 and 7, will be discussed in Appendix C in detail.

Appendix C: Ice number concentration for multi-modal polydisperse INP population

In PartMC, a particle population can consist of multiple modes. For each mode, its size distribution, species type and mass ratio, as well as number concentration are independently specified. Assuming that the total number of modes that form a group of INPs is N_{m}, and the size distribution density function for the INPs in the x^{th} mode is n_x, the size distribution density function for the entire INPs population is the sum of the density function across all modes, and the aggregate of the number concentrations from all modes equals the total number concentration of the entire INP group.

$$n_{\text{N}} = \sum_{x=1}^{N_{\text{m}}} n_x, \tag{C1}$$

$$\tilde{N}_{\text{t}} = \sum_{x=1}^{N_{\text{m}}} \tilde{N}_{\text{t}}^{(x)}. \tag{C2}$$

By substituting Eq. (C1) into Eq. (B6), and defining $\bar{\Phi}_{\text{x}}(t)$ as the weighted mean of the ice nucleation rate coefficient for the chemical components in the x^{th} mode, we derive a general formula for the size distribution density function of activated INPs in a population with multiple modes

$$n_{\text{frz}}(t,\, \ln D_{\text{p}}) = \sum_{x=1}^{N_x} n_x(t,\, \ln D_{\text{p}}) \cdot (1 - e^{-\pi D_{\text{p}}^2 \cdot \bar{\Phi}_{\text{x}}(t)}). \tag{C3}$$

Similarly, we can derive formulas for both the ice crystal number concentration and the frozen fraction for an INP population with multiple modes by substituting Eq. (C3) into Eq. (B7) and Eq. (B8),

$$\tilde{N}_{\text{frz}}(t) = \tilde{N}_{\text{t}} - \sum_{x=1}^{N_x} \int_{-\infty}^{+\infty} n_x(t,\, \ln D_{\text{p}}) \cdot e^{-\pi D_{\text{p}}^2 \cdot \bar{\Phi}_{\text{x}}(t)} d\ln D_{\text{p}}; \tag{C4}$$

$$f_{\text{frz}}(t) = 1 - \frac{1}{\tilde{N}_{\text{t}}} \cdot \sum_{x=1}^{N_x} \int_{-\infty}^{+\infty} n_x(t,\, \ln D_{\text{p}}) \cdot e^{-\pi D_{\text{p}}^2 \cdot \bar{\Phi}_{\text{x}}(t)} d\ln D_{\text{p}}. \tag{C5}$$

https://doi.org/10.5194/egusphere-2025-4326
Preprint. Discussion started: 24 September 2025

Assuming that the size of INPs in the x^{th} mode follows a log-normal distribution, characterized by a number concentration $\tilde{N}_{\text{t}}^{(x)}$, a geometric mean diameter $\bar{D}_{\text{pg}x}$, and a geometric standard deviation $\sigma_{\text{g}x}$, the size distribution density function for this mode is then given by

$$n_x(t, \ln D_{\text{p}}) = \frac{\tilde{N}_{\text{t}}^{(x)}}{\sqrt{2\pi} \cdot \ln \sigma_{\text{g}x}} e^{-\frac{(\ln D_{\text{p}} - \ln \bar{D}_{\text{pg}x})^2}{2\ln^2 \sigma_{\text{g}x}}}. \tag{C6}$$

Consequently, upon applying the assumption of a log-normal distribution for each mode, the calculations for ice crystal number concentration and frozen fraction are obtained by substituting Eq. (C6) into Eqs. (C4) and (C5), respectively.

$$\tilde{N}_{\text{frz}}(t) = \tilde{N}_{\text{t}} - \sum_{x=1}^{N_{\text{m}}} \frac{\tilde{N}_{\text{t}}^{(x)}}{\sqrt{2\pi} \cdot \ln \sigma_{\text{g}x}} \cdot \int_{-\infty}^{+\infty} \exp\left[-\frac{(\ln D_{\text{p}} - \ln \bar{D}_{\text{pg}x})^2}{2\ln^2 \sigma_{\text{g}x}} - \pi D_{\text{p}}^2 \cdot \bar{\Phi}_{\text{x}}(t) \right] d\ln D_{\text{p}}; \tag{C7}$$

$$f_{\text{frz}}(t) = 1 - \frac{1}{\tilde{N}_{\text{t}}} \sum_{x=1}^{N_{\text{m}}} \frac{\tilde{N}_{\text{t}}^{(x)}}{\sqrt{2\pi} \cdot \ln \sigma_{\text{g}x}} \cdot \int_{-\infty}^{+\infty} \exp\left[-\frac{(\ln D_{\text{p}} - \ln \bar{D}_{\text{pg}x})^2}{2\ln^2 \sigma_{\text{g}x}} - \pi D_{\text{p}}^2 \cdot \bar{\Phi}_{\text{x}}(t) \right] d\ln D_{\text{p}}. \tag{C8}$$

Based on the predefined parameters for the Cases 3 and 7, an externally mixed INP population in the PartMC model, composed of 50% illite and 50% Fe_2O_3, is created by establishing two modes. Each mode has an identical number concentration and size distribution, but differs in composition: one mode consists entirely of illite, while the other is composed solely of Fe_2O_3. Therefore, by establishing the parameters

$$\tilde{N}_{\text{t}}^{(1)} = \tilde{N}_{\text{t}}^{(2)} = \frac{1}{2} \cdot \tilde{N}_{\text{t}}; \tag{C9}$$

$$\bar{D}_{\text{pg1}} = \bar{D}_{\text{pg2}} = \bar{D}_{\text{pg}}; \tag{C10}$$

$$\sigma_{\text{g1}} = \sigma_{\text{g2}} = \sigma_{\text{g}}. \tag{C11}$$

and substituting Eq. (C9)–Eq. (C11) into Eq. (C7) and Eq. (C8), we derive formulas representing the ice crystal number concentration and frozen fraction for the Case 3 and 7 as

$$\begin{aligned} \tilde{N}_{\text{frz}}(t) = \tilde{N}_{\text{t}} - \frac{1}{2} \Bigg\{ & \frac{\tilde{N}_{\text{t}}}{\sqrt{2\pi} \cdot \ln \sigma_{\text{g}}} \cdot \int_{-\infty}^{+\infty} \exp\left[-\frac{(\ln D_{\text{p}} - \ln \bar{D}_{\text{pg}})^2}{2(\ln \sigma_{\text{g}})^2} - \pi D_{\text{p}}^2 \cdot \Phi_{\text{illite}}(T(t)) \right] d\ln D_{\text{p}} \\ & + \frac{\tilde{N}_{\text{t}}}{\sqrt{2\pi} \cdot \ln \sigma_{\text{g}}} \cdot \int_{-\infty}^{+\infty} \exp\left[-\frac{(\ln D_{\text{p}} - \ln \bar{D}_{\text{pg}})^2}{2(\ln \sigma_{\text{g}})^2} - \pi D_{\text{p}}^2 \cdot \Phi_{\text{Fe}_2\text{O}_3}(T(t)) \right] d\ln D_{\text{p}} \Bigg\}; \end{aligned} \tag{C12}$$

$$\begin{aligned} f_{\text{frz}}(t) = 1 - \frac{1}{2} \Bigg\{ & \frac{1}{\sqrt{2\pi} \cdot \ln \sigma_{\text{g}}} \cdot \int_{-\infty}^{+\infty} \exp\left[-\frac{(\ln D_{\text{p}} - \ln \bar{D}_{\text{pg}})^2}{2(\ln \sigma_{\text{g}})^2} - \pi D_{\text{p}}^2 \cdot \Phi_{\text{illite}}(T(t)) \right] d\ln D_{\text{p}} \\ & + \frac{1}{\sqrt{2\pi} \cdot \ln \sigma_{\text{g}}} \cdot \int_{-\infty}^{+\infty} \exp\left[-\frac{(\ln D_{\text{p}} - \ln \bar{D}_{\text{pg}})^2}{2(\ln \sigma_{\text{g}})^2} - \pi D_{\text{p}}^2 \cdot \Phi_{\text{Fe}_2\text{O}_3}(T(t)) \right] d\ln D_{\text{p}} \Bigg\}. \end{aligned} \tag{C13}$$

https://doi.org/10.5194/egusphere-2025-4326
Preprint. Discussion started: 24 September 2025

Table D1. Particle surface and surface fraction definitions and notations.

Symbol	Meaning
N_s	Number of species
N_p	Number of particles in population
i	Index of species, $i = 1, 2, ..., N_\mathrm{s}$
j	Index of particles, $j = 1, 2, ..., N_\mathrm{p}$
D_p	Dry diameter of particles (for monodisperse population)
$S_j^{(i)}$	Surface area of species i on the surface of particle j
S_{p_j}	$\sum_{i=1}^{N_\mathrm{s}} S_j^{(i)}$, total surface area of particle j
$S^{(i)}$	$\sum_{j=1}^{N_\mathrm{p}} S_j^{(i)}$, total surface area of species i in population
S_t	$\sum_{j=1}^{N_\mathrm{p}} S_{\mathrm{p}_j}$ (or $\sum_{i=1}^{N_\mathrm{s}} S^{(i)}$), total surface area of population
$w_j^{(i)}$	$\frac{S_j^{(i)}}{S_{\mathrm{p}_j}}$, surface fraction of species i on the surface of particle j
w_j	$\frac{S_{\mathrm{p}_j}}{S_\mathrm{t}}$, surface fraction of particle j in population
$w^{(i)}$	$\frac{S^{(i)}}{S_\mathrm{t}}$, surface fraction of species i in population
Φ_i	The Φ value of species i (defined by Eq. (8))

The terms $\Phi_{\mathrm{illite}}(T(t))$ and $\Phi_{\mathrm{Fe_2O_3}}(T(t))$ refer to the time integration of the ice nucleation rate coefficient of illite and Fe_2O_3, respectively.

Equations (C12) and (C13) provide the general formulas applicable to Cases 3 and 7, which differ in their respective temperature profiles, $T(t)$.

Appendix D: Proof of Theorem 1

The symbols used in this proof are listed in the Table D1.

Based on the definitions in Table D1, there are:

$$\sum_{i=1}^{N_\mathrm{s}} w_j^{(i)} = 1, \text{ for } \forall j \in [1, N_\mathrm{p}] \tag{D1}$$

$$\sum_{j=1}^{N_\mathrm{p}} S_{\mathrm{p}_j} w_j^{(i)} = \sum_{j=1}^{N_\mathrm{p}} \pi D_\mathrm{p}^2 w_j^{(i)} = S^{(i)}, \text{ for } \forall i \in [1, N_\mathrm{s}] \tag{D2}$$

$$0 \le w_j^{(i)} \le 1, \text{ for } \forall i \in [1, N_\mathrm{s}], \forall j \in [1, N_\mathrm{p}]. \tag{D3}$$

A series of $w_j^{(i)}$ must satisfies Eqs. (D1), (D2), and (D3) to represent a meaningful mixing state.

https://doi.org/10.5194/egusphere-2025-4326
Preprint. Discussion started: 24 September 2025

Here are the assumptions in this proof: First: $S^{(i)}$, $i = 1, 2, ..., N_s$ are constants, and satisfying $\sum_{i=1}^{N_s} S^{(i)} = \pi D_p^2 N_p$ to make sure the sum of each species' total surface equals the sum of particle's surface. Second: For each species i ($i = 1, 2, ..., N_s$), $\frac{S^{(i)}}{\pi D_p^2}$ is an integer to make sure each species covers an integer number of particle in the external mixture. Third: Assume $\Phi_1 \neq \Phi_2 \neq ... \neq \Phi_{N_s}$ to avoid some mathematical complexity, if two species do have the same Φ value, just regard them as the same species, which would not affect our result.

We divide the proof of Theorem 1 into two parts — Theorem 1A and Theorem 1B — which demonstrate that the internal mixture is the most efficient mixing state and the external mixture is the least efficient, respectively.

Theorem 1A. *For monodisperse INP populations, the internal mixture is the most efficient mixing state.*

Proof. The topic of the most efficient mixing state in terms of frozen fraction can be converted to an optimization problem:

optimization 1

$$\max_{w_j^{(i)} \in [0,1]} 1 - \frac{1}{N_p} \sum_{j=1}^{N_p} \exp\left(-\pi D_p^2 \sum_{i=1}^{N_s} w_j^{(i)} \Phi_i\right) \tag{D4}$$

$$s.t. \sum_{i=1}^{N_s} w_j^{(i)} = 1 \tag{D5}$$

$$\sum_{j=1}^{N_p} w_j^{(i)} = \frac{S^{(i)}}{\pi D_p^2} \tag{D6}$$

Define $f_{frz}^{(max)}$ as the maximum solution of optimization 1. Since $\exp\left(-\pi D_p^2 \cdot \sum_{i=1}^{N_s} w_j^{(i)} \Phi_i\right) = P_{unf,j}$, combining with Eq. (D2), there is:

$$\prod_{j=1}^{N_p} P_{unf,j} = \prod_{j=1}^{N_p} \exp\left(-\pi D_p^2 \sum_{i=1}^{N_s} w_j^{(i)} \Phi_i\right) = \exp\left(-\pi D_p^2 \sum_{j=1}^{N_p} \sum_{i=1}^{N_s} w_j^{(i)} \Phi_i\right) \tag{D7}$$

$$= \exp\left[-\sum_{i=1}^{N_s} \Phi_i \cdot \left(\pi D_p^2 \cdot \sum_{j=1}^{N_s} w_j^{(i)}\right)\right] = \exp\left(-\sum_{i=1}^{N_s} S^{(i)} \Phi_i\right) = \text{constant}. \tag{D8}$$

We therefore define a constant:

$$\mathcal{K} = \exp\left(-\sum_{i=1}^{N_s} S^{(i)} \Phi_i\right), \tag{D9}$$

we can propose another optimization problem:

optimization 2

$$\max_{P_{unf,j} \in [0,1]} 1 - \frac{1}{N_p} \sum_{j=1}^{N_p} P_{unf,j} \tag{D10}$$

https://doi.org/10.5194/egusphere-2025-4326
Preprint. Discussion started: 24 September 2025

$$s.t. \prod_{j=1}^{N_\mathrm{p}} P_{\mathrm{unf},j} = \mathcal{K} \tag{D11}$$

and define f^*_{frz} is the solution of this problem. It is worth noting that since there are

$$1 - \frac{1}{N_\mathrm{p}} \sum_{j=1}^{N_\mathrm{p}} \exp\left(-\pi D_\mathrm{p}^2 \sum_{i=1}^{N_\mathrm{s}} w_j^{(i)} \Phi_i\right) \equiv 1 - \frac{1}{N_\mathrm{p}} \sum_{j=1}^{N_\mathrm{p}} P_{\mathrm{unf},j}, \tag{D12}$$

$$\sum_{j=1}^{N_\mathrm{p}} w_j^{(i)} = \frac{S^{(i)}}{\pi D_\mathrm{p}^2} \Leftrightarrow \prod_{j=1}^{N_\mathrm{p}} P_{\mathrm{unf},j} = \mathcal{K}, \tag{D13}$$

the optimization 2 only lost the constraint of Eq. (D5) , therefore, there is

$$f^*_{\mathrm{frz}} \geq f^{(\max)}_{\mathrm{frz}}. \tag{D14}$$

Now, we solve optimization 2, using the Lagrange multiplier, define

$$L\left(P_{\mathrm{unf},1}, P_{\mathrm{unf},2}, ..., P_{\mathrm{unf},N_\mathrm{p}}\right) = 1 - \frac{1}{N_\mathrm{p}} \sum_{j=1}^{N_\mathrm{p}} P_{\mathrm{unf},j} + \lambda \left(\prod_{j=1}^{N_\mathrm{p}} P_{\mathrm{unf},j} - \mathcal{K}\right), \tag{D15}$$

and define $P^*_{\mathrm{unf},1}, P^*_{\mathrm{unf},2}, ..., P^*_{\mathrm{unf},N_\mathrm{p}}, \lambda^*$ is the solution that maximize the function L. There are

$$\left.\frac{\partial L}{\partial P_{\mathrm{unf},j}}\right|_{P_{\mathrm{unf},j}=P^*_{\mathrm{unf},j}} = -\frac{1}{N_\mathrm{p}} + \lambda^* \prod_{j'=1, j'\neq j}^{N_\mathrm{p}} P^*_{\mathrm{unf},j'} = 0, \text{ for } \forall j \in [1, N_\mathrm{p}], \tag{D16}$$

$$\left.\frac{\partial L}{\partial \lambda}\right|_{\lambda=\lambda^*} = \prod_{j'=1}^{N_\mathrm{p}} P^*_{\mathrm{unf},j'} - \mathcal{K} = 0. \tag{D17}$$

Substitute Eq. (D17) into Eq. (D16) for each $j \in [1, N_\mathrm{p}]$, we have

$$-\frac{1}{N_\mathrm{p}} + \lambda^* \cdot \frac{\mathcal{K}}{P^*_{\mathrm{unf},j}} = 0 \Leftrightarrow P^*_{\mathrm{unf},j} = N_\mathrm{p} \lambda^* \cdot \mathcal{K} \text{ for } \forall j \in [1, N_\mathrm{p}]. \tag{D18}$$

Substitute Eq. (D18) into Eq. (D17), we have

$$\left(N_\mathrm{p} \lambda^* \cdot \mathcal{K}\right)^{N_\mathrm{p}} = \mathcal{K} \Leftrightarrow \lambda^* = \frac{1}{N_\mathrm{p}} \cdot \mathcal{K}^{\frac{1}{N_\mathrm{p}}-1}. \tag{D19}$$

Substitute Eq. (D19) into Eq. (D18), we have

$$P^*_{\mathrm{unf},j} = \mathcal{K}^{\frac{1}{N_\mathrm{p}}} = \exp\left(-\frac{1}{N_\mathrm{p}} \sum_{i=1}^{N_\mathrm{p}} S^{(i)} \Phi_i\right), \text{ for } \forall j \in [1, N_\mathrm{p}]. \tag{D20}$$

https://doi.org/10.5194/egusphere-2025-4326
Preprint. Discussion started: 24 September 2025

Therefore, when each particle has the same unfrozen (or freezing) probability, the Eq. (D10) in optimization 2 reach the maximum, where

$$f_{\mathrm{frz}}^{*} = 1 - \sum_{j=1}^{N_{\mathrm{p}}} P_{\mathrm{unf},j}^{*} = 1 - \exp\left(-\frac{1}{N_{\mathrm{p}}} \sum_{i=1}^{N_{\mathrm{s}}} S^{(i)} \Phi_i\right). \tag{D21}$$

For the internal mixture, which, defined in Riemer and West (2013), satisfies

$$w_j^{(i)} = \frac{S^{(i)}}{\pi D_{\mathrm{p}}^2 N_{\mathrm{p}}} \text{ for } \forall j \in [1, N_{\mathrm{p}}], \forall i \in [1, N_{\mathrm{s}}]. \tag{D22}$$

Define the frozen fraction of internal mixture is $f_{\mathrm{frz}}^{(\mathrm{int})}$, there is

$$\begin{aligned} f_{\mathrm{frz}}^{(\mathrm{int})} &= 1 - \frac{1}{N_{\mathrm{p}}} \sum_{j=1}^{N_{\mathrm{p}}} \exp\left(-\pi D_{\mathrm{p}}^2 \cdot \sum_{i=1}^{N_{\mathrm{s}}} w_j^{(i)} \Phi_i\right) \\ &= 1 - \frac{1}{N_{\mathrm{p}}} \sum_{j=1}^{N_{\mathrm{p}}} \exp\left(-\pi D_{\mathrm{p}}^2 \cdot \sum_{i=1}^{N_{\mathrm{s}}} \frac{S^{(i)}}{\pi D_{\mathrm{p}}^2 N_{\mathrm{p}}} \cdot \Phi_i\right) = 1 - \exp\left(-\frac{1}{N_{\mathrm{p}}} \sum_{i=1}^{N_{\mathrm{s}}} S^{(i)} \Phi_i\right), \end{aligned} \tag{D23}$$

therefore, $f_{\mathrm{frz}}^{(\mathrm{int})} = f_{\mathrm{frz}}^{*}$. In addition, since the internal mixture shown in Eq. (D22) satisfies the constraints in optimization 1 (Eqs. (D5) and (D6)), thus, there must be

$$f_{\mathrm{frz}}^{(\mathrm{int})} = f_{\mathrm{frz}}^{*} \leq f_{\mathrm{frz}}^{(\mathrm{max})}, \tag{D24}$$

combining Eq. (D14), we have:

$$f_{\mathrm{frz}}^{(\mathrm{int})} = f_{\mathrm{frz}}^{*} = f_{\mathrm{frz}}^{(\mathrm{max})}. \tag{D25}$$

Therefore, the internal mixture is the most efficient mixing state for monodisperse particle population.

Theorem 1B. *For monodisperse INP populations, the external mixture is the least efficient mixing state.*

Proof. According to the definition of external mixture in Riemer and West (2013), there is

$$\text{External mixture} \Leftrightarrow w_j^{(i)} = 0 \text{ or } 1, \sum_{i=1}^{N_{\mathrm{s}}} w_j^{(i)} = 1, \text{ for } \forall i \in [1, N_{\mathrm{s}}], \forall j \in [1, N_{\mathrm{p}}].$$

Define the frozen fraction of external mixture is denoted as $f_{\mathrm{frz}}^{(\mathrm{ext})}$, based on Eq. (12), we have

$$f_{\mathrm{frz}}^{(\mathrm{ext})} = 1 - \sum_{i=1}^{N_{\mathrm{s}}} w^{(i)} P_{\mathrm{unf},j} = 1 - \sum_{i=1}^{N_{\mathrm{s}}} \frac{S^{(i)}}{\pi D_{\mathrm{p}}^2 N_{\mathrm{p}}} \cdot \exp\left(-\pi D_{\mathrm{p}}^2 \Phi_i\right). \tag{D26}$$

We prove the theorem 1B by contradiction. Assuming a mixing state of monodisperse particle population, described by $\tilde{w}_j^{(i)}$, $i = 1, 2, ..., N_{\mathrm{s}}$, $j = 1, 2, ..., N_{\mathrm{p}}$, is the least efficient mixing state but is not the external mixture. Define the frozen fraction

$$\tilde{f}_{\mathrm{frz}} = 1 - \frac{1}{N_{\mathrm{p}}} \sum_{j=1}^{N_{\mathrm{p}}} \exp\left(-\pi D_{\mathrm{p}}^2 \sum_{i=1}^{N_{\mathrm{s}}} \tilde{w}_j^{(i)} \Phi_i\right). \tag{D27}$$

https://doi.org/10.5194/egusphere-2025-4326
Preprint. Discussion started: 24 September 2025

Since it is different with external mixture, there must be

$$\exists i \in [1, N_\mathrm{s}], \exists j \in [1, N_\mathrm{p}], 0 < \tilde{w}_j^{(i)} < 1,$$

in other words, define the set $\tilde{M}_{ix} = \left\{ i \middle| \exists j \in [1, N_\mathrm{p}], 0 < \tilde{w}_j^{(i)} < 1 \right\}$, there must be $\tilde{M}_{ix} \neq \emptyset$. Define $i_0 = \arg\min_{i \in \tilde{M}_{ix}} \Phi_i$, there is $\exists j_A \in [1, N_\mathrm{p}], 0 < \tilde{w}_{j_A}^{(i_0)} < 1$, by the definition of $\tilde{M}_{ix}$. According to the assumption of $\frac{S_{i_0}}{\pi D_\mathrm{p}^2}$ is an integer, there must be $\exists j_B \in [1, N_\mathrm{p}]$, $j_B \neq j_A$, and $0 < \tilde{w}_{j_B}^{(i_0)} < 1$, otherwise, $\sum_{j=1, j\neq j_A}^{N_\mathrm{p}} \tilde{w}_j^{(i_0)}$ must be an integer and $\frac{S_{i_0}}{\pi D_\mathrm{p}^2} = \frac{\sum_{j=1}^{N_\mathrm{p}} \tilde{w}_j^{(i_0)} \cdot \pi D_\mathrm{p}^2}{\pi D_\mathrm{p}^2} = \sum_{j=1}^{N_\mathrm{p}} \tilde{w}_j^{(i_0)} = \tilde{w}_{j_A}^{(i_0)} + \sum_{j=1, j\neq j_A}^{N_\mathrm{p}} \tilde{w}_j^{(i_0)}$ would not be an integer.

We assume $P_{\mathrm{unf},j_A} \geq P_{\mathrm{unf},j_B}$, if not, we can just switch the index of j_A and j_B for these two particles. Now, we look at the particle j_A and j_B, define $A_{j_A} = \left\{ i \middle| \tilde{w}_{j_A}^{(i)} > 0, i \in [1, N_\mathrm{s}] \right\}$, $A_{j_B} = \left\{ i \middle| \tilde{w}_{j_B}^{(i)} > 0, i \in [1, N_\mathrm{s}] \right\}$, are the set of species index that particle A and B contains, respectively. Since $0 < \tilde{w}_{j_A}^{(i_0)} < 1$ and $\sum_{i=1}^{N_\mathrm{s}} \tilde{w}_{j_A}^{(i)} = 1$, for $\forall i_A \in A_{j_A}$, there is $0 < \tilde{w}_{j_A}^{(i_A)} < 1$, therefore, for $\forall i_A \in A_{j_A}$, $i_A \in \tilde{M}_{ix}$, and there is $\Phi_{i_0} < \Phi_{i_A}$ according to the definition of i_0. Similarly, there also be $\forall i_B \in A_{j_B}$, $i_B \in \tilde{M}_{ix}$, and $\Phi_{i_0} < \Phi_{i_B}$. This implies that, when we define

$$\bar{\Phi}_{j_A}^{(i\neq i_0)} = \frac{1}{\sum_{i=1, i\neq i_0}^{N_\mathrm{s}} \tilde{w}_{j_A}^{(i)}} \sum_{i=1, i\neq i_0}^{N_\mathrm{s}} \tilde{w}_{j_A}^{(i)} \Phi_i, \tag{D28}$$

there must be $\Phi_{i_0} < \bar{\Phi}_{j_A}^{(i\neq i_0)}$.

Now, we construct a new mixing state, described as $\hat{w}_j^{(i)}$, $i = 1, 2, ..., N_\mathrm{s}$, $j = 1, 2, .., N_\mathrm{p}$, such that

$$\hat{w}_j^{(i)} = \begin{cases} \tilde{w}_{j_A}^{(i_0)} + \delta w, & j = j_A, i = i_0; \\ \tilde{w}_{j_A}^{(i)} - \delta w \cdot \frac{\tilde{w}_{j_A}^{(i)}}{\sum_{i'=1, i'\neq i_0}^{N_\mathrm{s}} \tilde{w}_{j_A}^{(i)}}, & j = j_A, i \neq i_0; \\ \tilde{w}_{j_B}^{(i_0)} - \delta w, & j = j_B, i = i_0; \\ \tilde{w}_{j_B}^{(i)} + \delta w \cdot \frac{\tilde{w}_{j_A}^{(i)}}{\sum_{i'=1, i'\neq i_0}^{N_\mathrm{s}} \tilde{w}_{j_A}^{(i)}}, & j = j_B, i \neq i_0; \\ \tilde{w}_j^{(i)}, & j \neq j_A, j \neq j_B, \end{cases} \tag{D29}$$

where $\delta w = \min\left\{ \tilde{w}_{j_A}^{(i_0)}, 1 - \tilde{w}_{j_A}^{(i_0)}, \tilde{w}_{j_B}^{(i_0)}, 1 - \tilde{w}_{j_B}^{(i_0)} \right\}$ (satisfies $0 < \delta w < 1$). Noting that there are $\sum_{i=1}^{N_\mathrm{s}} \hat{w}_j^{(i)} = \sum_{i=1}^{N_\mathrm{s}} \tilde{w}_j^{(i)} = 1$, for $\forall j \in [1, N_\mathrm{p}]$, $\sum_{j=1}^{N_\mathrm{p}} \hat{w}_j^{(i)} = \sum_{j=1}^{N_\mathrm{p}} \tilde{w}_j^{(i)} = \frac{S^{(i)}}{\pi D_\mathrm{p}^2}$, for $\forall i \in [1, N_\mathrm{s}]$, and $0 \leq \tilde{w}_j^{(i)} \leq 1$ for $\forall i \in [1, N_\mathrm{s}]$, $\forall j \in [1, N_\mathrm{p}]$, which indicates Eq. (D29) represent a meaningful mixing state (satisfying Eqs. (D1), (D2), and (D3)).

Define

$$\hat{P}_{\mathrm{unf},j} = \exp\left(-\pi D_\mathrm{p}^2 \cdot \sum_{i=1}^{N_\mathrm{s}} \hat{w}_j^{(i)} \Phi_i \right) \tag{D30}$$

https://doi.org/10.5194/egusphere-2025-4326
Preprint. Discussion started: 24 September 2025

is the unfrozen probability of j^{th} particle in the mixing state represented by $\hat{w}_j^{(i)}$, define

$$\tilde{P}_{\text{unf},j} = \exp\left(-\pi D_{\text{p}}^2 \cdot \sum_{i=1}^{N_{\text{s}}} \tilde{w}_j^{(i)} \Phi_i\right) \tag{D31}$$

is the unfrozen probability of j^{th} particle in the mixing state represented by $\tilde{w}_j^{(i)}$. Substituting Eqs. (D29) and (D28) into Eq. (D30) and combining with Eq. (D31), there is

$$\hat{P}_{\text{unf},j} = \begin{cases} \tilde{P}_{\text{unf},j_A} \cdot \exp\left[\pi D_{\text{p}}^2 \delta w \cdot \left(\bar{\Phi}_{j_A}^{(i\neq i_0)} - \Phi_{i_0}\right)\right], & j = j_A; \\ \tilde{P}_{\text{unf},j_B} \cdot \exp\left[-\pi D_{\text{p}}^2 \delta w \cdot \left(\bar{\Phi}_{j_A}^{(i\neq i_0)} - \Phi_{i_0}\right)\right], & j = j_B; \\ \tilde{P}_{\text{unf},j}, & j \neq j_A, j \neq j_B. \end{cases} \tag{D32}$$

Therefore, according to Eq. (D32), we have

$$\hat{P}_{\text{unf},j_A} + \hat{P}_{\text{unf},j_B} - \tilde{P}_{\text{unf},j_A} - \tilde{P}_{\text{unf},j_B} = \tilde{P}_{\text{unf},j_A} \cdot \left(e^{\delta\phi} - 1\right) - \tilde{P}_{\text{unf},j_B} \cdot \left(1 - e^{-\delta\phi}\right), \tag{D33}$$

where $\delta\phi = \pi D_{\text{p}}^2 \delta w \cdot \left(\bar{\Phi}_{j_A}^{(i\neq i_0)} - \Phi_{i_0}\right)$. Nothing that since $\Phi_{i_0} < \bar{\Phi}_{j_A}^{(i\neq i_0)}$, there is $\delta\phi > 0$, thus, $e^{\delta\phi} - 1 > 0$ and $1 - e^{-\delta\phi} > 0$. Since $\tilde{P}_{\text{unf},j_A} \geq \tilde{P}_{\text{unf},j_B}$, there is

$$\begin{aligned} \hat{P}_{\text{unf},j_A} + \hat{P}_{\text{unf},j_B} - \tilde{P}_{\text{unf},j_A} - \tilde{P}_{\text{unf},j_B} &= \tilde{P}_{\text{unf},j_A} \cdot \left(e^{\delta\phi} - 1\right) - \tilde{P}_{\text{unf},j_B} \cdot \left(1 - e^{-\delta\phi}\right) \\ &\geq \tilde{P}_{\text{unf},j_B} \cdot \left(e^{\delta\phi} - 1\right) - \tilde{P}_{\text{unf},j_B} \cdot \left(1 - e^{-\delta\phi}\right) \\ &= \tilde{P}_{\text{unf},j_B} \cdot \left(e^{\delta\phi} + e^{-\delta\phi} - 2\right) > 0, \end{aligned} \tag{D34}$$

therefore, we have

$$\hat{P}_{\text{unf},j_A} + \hat{P}_{\text{unf},j_B} > \tilde{P}_{\text{unf},j_A} + \tilde{P}_{\text{unf},j_B}. \tag{D35}$$

The frozen fraction of the new mixing state represented by Eq. (D29) is

$$\begin{aligned} \hat{f}_{\text{frz}} &= 1 - \frac{1}{N_{\text{p}}} \left(\hat{P}_{\text{unf},j_A} + \hat{P}_{\text{unf},j_B} + \sum_{j=1, j\neq j_A, j\neq j_B}^{N_{\text{p}}} \hat{P}_{\text{unf},j}\right) \\ &< 1 - \frac{1}{N_{\text{p}}} \left(\tilde{P}_{\text{unf},j_A} + \tilde{P}_{\text{unf},j_B} + \sum_{j=1, j\neq j_A, j\neq j_B}^{N_{\text{p}}} \tilde{P}_{\text{unf},j}\right) \\ &= 1 - \frac{1}{N_{\text{p}}} \sum_{j=1}^{N_{\text{p}}} \tilde{P}_{\text{unf},j} = \tilde{f}_{\text{frz}}. \end{aligned} \tag{D36}$$

This implies the mixing state represented by $\hat{w}_j^{(i)}$ in Eq. (D29) has a smaller frozen fraction than the mixing state represented by $\tilde{w}_j^{(i)}$, which conflicts with the least efficient mixing state assumption. We thus prove that for monodisperse INP population, any mixing state other than the external mixture cannot be the least efficient mixing state, because we can always construct another mixing state using Eq. (D29), which always has a lower frozen fraction. Therefore, the external mixture is the least efficient mixing state for monodisperse INPs.

https://doi.org/10.5194/egusphere-2025-4326
Preprint. Discussion started: 24 September 2025

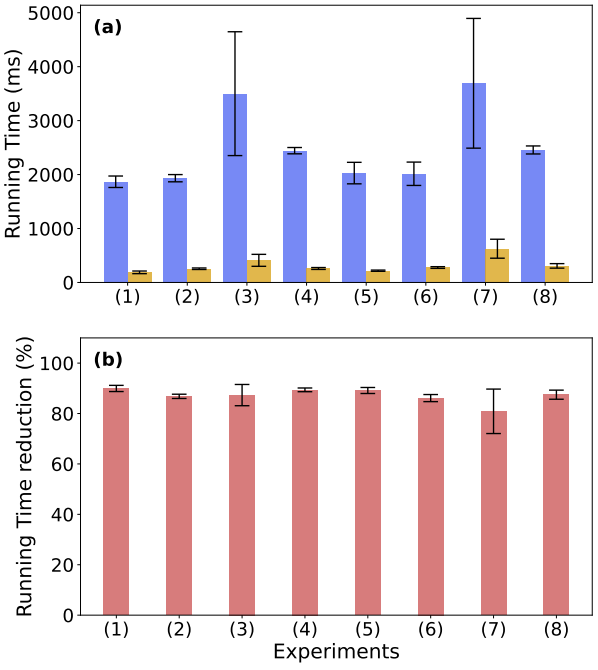

Figure E1. Runtime reductions for naive and accelerated algorithms. Panel (a) shows the running times of the naive (blue) and accelerated (orange) algorithms across eight different experiments. Panel (b) depicts the percentage of time reduction achieved by the accelerated algorithm in each run. Error bars represent the standard deviation of run times, indicating variability in simulation times across 20 trials.

Appendix E: Efficiency and exactness of the accelerated algorithm

In this appendix, the terms "naive algorithm" and "accelerated algorithm" refer to algorithm 2 and algorithm 3 in section 4.3, respectively. Figure E1 compares the run time and efficiency gains for the naive and accelerated algorithms for the eight cases listed in Table 2. The performance metrics were obtained from 20 independent trials for each case, evaluating both algorithms separately. The run times reflect exclusively the immersion freezing process. Other aspects such as model initialization, file input/output operations, and simulations of other physical processes are excluded from this evaluation. All tests were conducted on a single core of the Keeling computer cluster at the University of Illinois at Urbana-Champaign.

The accelerated algorithm reduces the run time on average by 87.26%, which is equivalent to a x7.85 speed up.

In the context of the tau-leaping algorithm, when the simulation involves particles with less effective INPs, the majority of these INPs are bypassed during the tau-leaping steps. This suggests that the accelerated algorithm is more efficient in simulating the freezing process of particles with lower-efficiency INPs. However, since each particle can only undergo one freezing event before melting, and if the temperature remains below 0 °C, both the naive and accelerated algorithms will only account for particles that remain unfrozen. Particles containing more effective INPs exhibit a higher freezing ratio, resulting in fewer unfrozen particles. Consequently, as the algorithm iterates over a diminishing pool of unfrozen particles, the computational

https://doi.org/10.5194/egusphere-2025-4326
Preprint. Discussion started: 24 September 2025

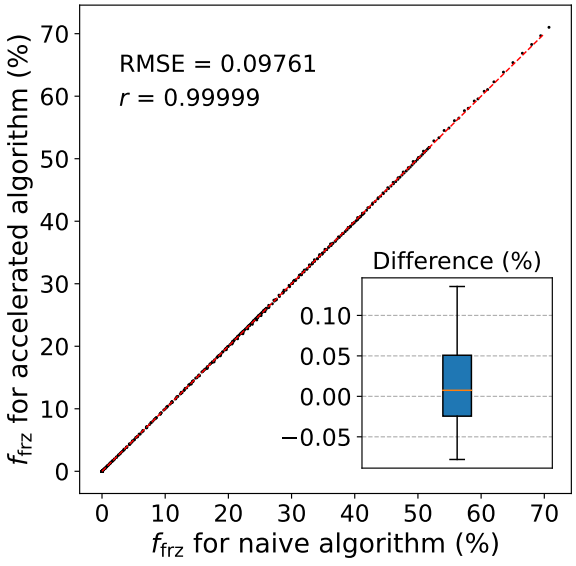

Figure E2. Average frozen fraction at 10-second intervals from eight experiments as obtained by the naive and accelerated algorithms. Each data point is the mean of 20 trials per experiment, showing the precision of the accelerated algorithm in simulating the freezing process. The red dashed line represents a one-to-one correlation. The inset boxplot illustrates the maximum, 75th percentile, median, 25th percentile, and minimum of the f_{frz} differences between the accelerated and naive algorithms.

running time is reduced. Thus, simulating the freezing of particles with highly efficient INPs can lead to run-time efficiencies in this manner. These competing effects may partially account for the insignificant variations in run time reduction observed across different INP groups, as shown in the panel b of Fig. E1.

Figure E2 presents a comparison of the frozen fraction results simulated by the naive and accelerated algorithms. The outcomes from both algorithms are closely aligned, with a correlation coefficient exceeding 0.999 and a mean square root error (RMSE) of just 0.098 (expressed as a percentage). These minor discrepancies are entirely justifiable, considering the inherent stochastic variance expected from random algorithms and underscore the robustness of the accelerated algorithm.

The method of grouping particles into bins and the approach used to calculate the $P_i^{\max}$ for each bin can significantly influence the algorithm's efficiency. If there is a large variance in the selection probability of particles within the same bin—meaning the upper bound value, $P_i^{\max}$, is substantially higher than the selection probabilities for the majority of particles in that bin, the algorithm's efficiency decreases. This scenario occurs when factors other than particle size affect their selection probability.

In the context of immersion freezing simulations for single-species INPs, variation in freezing probabilities are solely due to size differences, as all INPs are of the same species and are exposed to the same environmental conditions. The PartMC model groups particles by size, ensuring that INPs within the same bin are similarly sized and, therefore, have comparable freezing

https://doi.org/10.5194/egusphere-2025-4326
Preprint. Discussion started: 24 September 2025

probabilities. However, for externally mixed INP collections, such as Cases 3 and 7, to make sure $P_i^{\max}$ is the upper bound of the freezing probability within the i^{th} bin, it is calculated by $P_i^{\max} = 1 - \exp\left(-S_{\text{p},i}^{(\max)} \cdot J_{\text{het}}^{(\max)} \cdot \Delta t\right)$, where $S_{\text{p},i}^{(\max)}$ is the surface area of the largest particle over that bin, $J_{\text{het}}^{(\max)}$ is the ice nucleation rate coefficient of the most efficient species, and Δt is the time interval during the simulation. This can lead to a large overestimation of the real freezing probability for INPs only covered by less efficient species within that bin. In the Cases 3 and 7, the algorithm selects many illite particles using the maximum freezing probability of Fe_2O_3 particle during tau-leaping, and then rejects most of them in the secondary selection. For example, in case 7 at 600 s, where the temperature is $-30\,^{\circ}\text{C}$, the ice nucleating rate coefficients are $J_{\text{het}}^{(\text{Fe}_2\text{O}_3)} = 7.85 \times 10^9\ \text{m}^{-2}\ \text{s}^{-1}$ and $J_{\text{het}}^{(\text{illite})} = 1.42 \times 10^7\ \text{m}^{-2}\ \text{s}^{-1}$. Consider the i^{th} bin containing particles with dry diameters ranging from 1 µm to 1.1 µm, and assume $\Delta t = 1$ s. The maximum freezing probability in this bin is $P_i^{\max} = 0.0294$. However, the actual freezing probability for illite particles of 1 µm diameter is only 4.48×10^{-5}—656 times smaller than $P_i^{\max}$. This implies that, out of 100,000 unfrozen computational particles, the tau-leaping algorithm would initially select approximately 2940 particles, yet only 4 to 5 particles would remain after the secondary selection. This inefficient process increases the run time and results in a relatively lower run time reduction, as shown in Fig. E1. Even so, in Case 3 and Case 7, the binned tau-leaping algorithm still saved over 80% of computation time on average compared to the naive algorithm. Using the binned tau-leaping algorithm remains a better choice. A potential solution to this issue is to group INPs by both size and modes, where we assume aerosols are internally mixed within each mode. This bin structure ensures that particles within each bin are of the same species and similar size, Consequently, the $P_i^{\max}$ would not excessively exceed the probabilities of most particles in the bin, potentially enhancing the algorithm's overall efficiency. However, maintaining a two-dimensional bin structure would come with additional computational cost.

Appendix F: Definition of χ index with respect to surface

The definition of χ index with respect to species surface is defined in Table F1, while the mathematical signs are defined in Table D1. Definition is similar to that of Riemer and West (2013), the only difference is using the surface ratio in stead of the mass fraction.

Appendix G: Method for generating the INP population with specific mixing state

The objective of this method is to generate an INP population in which particles within each size bin exhibit an intermediate mixing state defined by a prescribed χ value. We begin by initializing two separate INP populations composed entirely of pure Fe_2O_3 and pure illite, respectively, both sharing the same size distribution. By combining these two populations, we obtain an externally mixed INP population with $\chi = 0\%$.

Next, we divide the combined population into 100 size bins. Within each bin, we iteratively introduce mixing as follows: two particles (e.g., particles j_1 and j_2) are randomly selected, and a surface area S_{e} is randomly generated from a uniform distribution between 0 and $< \min\left\{S_{\text{p}_{j_1}}, S_{\text{p}_{j_2}}\right\}$. We then exchange this surface area between the two particles, assuming that the species surface ratio of the transferred surface segment from particle j_1 to particle j_2 is the same as species surface ratio of

https://doi.org/10.5194/egusphere-2025-4326
Preprint. Discussion started: 24 September 2025

Table F1. Definitions of aerosol mixing entropies, particle diversities, and mixing state index. In these definitions we take $0 \ln 0 = 0$ and $0^0 = 1$. The definition and naming of the quantities are based on Riemer and West (2013).

Quantity	Name	Meaning
$H_j = \sum_{i=1}^{N_s} -w_j^{(i)} \ln w_j^{(i)}$	mixing entropy of particle j	Shannon entropy of species distribution within particle j
$H_\alpha = \sum_{j=1}^{N_p} w_j H_j$	average particle mixing entropy	average Shannon entropy per particle
$H_\gamma = \sum_{i=1}^{N_s} -w^{(i)} \ln w^{(i)}$	population bulk mixing entropy	Shannon entropy of species distribution within population
$D_j = e^{H_j} = \prod_{i=1}^{N_s} \left(w_j^{(i)}\right)^{-w_j^{(i)}}$	particle diversity of particle j	effective number of species in particle j
$D_\alpha = e^{H_\alpha} = \prod_{j=1}^{N_p} (D_j)^{w_j}$	average particle (alpha) species diversity	average effective number of species in each particle
$D_\gamma = e^{H_\gamma} = \prod_{i=1}^{N_s} \left(w^{(i)}\right)^{-w^{(i)}}$	bulk population (gamma) species diversity	effective number of species in the population
$D_\beta = \frac{D_\gamma}{D_\alpha}$	inter-particle (beta) diversity	amount of population species diversity due to inter-particle diversity
$\chi = \frac{D_\alpha - 1}{D_\gamma - 1}$	mixing state index	degree to which population is externally mixed ($\chi = 0\%$) versus internally mixed (χ=100%)

particle j_1, and the species surface ratio of the transferred surface segment from particle j_2 to particle j_1 is the same as species surface ratio of particle j_2.

This exchange process incrementally increases the degree of mixing within the bin, and consequently, the χ value. The selection and exchange steps are repeated until the χ value of the bin reaches the prescribed target. This procedure is applied independently across all bins, ensuring that particles within each bin attain the desired intermediate mixing state characterized by the specified χ.

Algorithm G1 summarizes the procedure described above. The mixing state is represented by a two-dimensional array $M[1 : N_s, 1 : N_p]$, where $M[i, j]$ denotes the fractional surface area of the j^{th} particle covered by the i^{th} species. Particle sizes are stored in a surface area array $S_p[1 : N_p]$, where $S_p[j]$ corresponds to the surface area of the j^{th} particle. The prescribed mixing state is defined by the target χ value, denoted as χ_{obj}.

Author contributions. WT led the conceptualization, implemented the modeling framework, conducted the simulations, and wrote the first draft of the manuscript. NR provided primary guidance on the conceptual development and contributed extensively to the writing and revision of the manuscript. DAK and MW contributed to the conceptual framing of the study and provided input on manuscript revision. SA developed

https://doi.org/10.5194/egusphere-2025-4326
Preprint. Discussion started: 24 September 2025

Algorithm G1 Random surface exchange method (method of initializing an intermediate mixing state)

Initializing an INP population π with external mixture, each type of INP has the same size distribution
Grouping π to N_{bin} number of bins, $\pi_1, \pi_2, ..., \pi_{N_{\text{bin}}}$.
for $k = 1,\ 2,\ \ldots,\ N_{\text{bin}}$ **do**
  loop
    Randomly select $j_1, j_2 \in \pi_i$
    $r = randUnif()$
    $S_{\text{e}} = r \cdot \min\{S_{\text{p}}[j_1], S_{\text{p}}[j_2]\}$
    $M[:, j_1] = M[:, j_1] + \frac{1}{S_{\text{p}}[j_1]}\{-S_{\text{e}} \cdot M[:, j_1] + S_{\text{e}} \cdot M[:, j_2]\}$
    $M[:, j_2] = M[:, j_2] + \frac{1}{S_{\text{p}}[j_2]}\{-S_{\text{e}} \cdot M[:, j_2] + S_{\text{e}} \cdot M[:, j_1]\}$
    Calculate χ_k for π_k.
    if $\chi_k \geq \chi_{\text{obj}}$ **then**
      break
    end if
  end loop
end for

the initial version of the modeling code and contributed significantly to the manuscript draft. JHC and MW assisted with code development and provided feedback on the analysis and writing. All authors discussed the results and contributed to the final version of the manuscript.

Competing interests. At least one of the (co-)authors is a member of the editorial board of Atmospheric Chemistry and Physics.

Acknowledgements. This research was supported by the Department of Energy, Atmospheric System Research (ASR), under Grants DE-SC0021034 and DE-SC0022130 and by the National Science Foundation under Grant AGS 23-22857. All authors gratefully acknowledge the funding sources listed above.

https://doi.org/10.5194/egusphere-2025-4326
Preprint. Discussion started: 24 September 2025

References

Abade, G. C. and Albuquerque, D. G.: Persistent mixed-phase states in adiabatic cloud parcels under idealised conditions, Quarterly Journal of the Royal Meteorological Society, 150, 3450–3474, https://doi.org/10.1002/qj.4775, 2024.

Adachi, K., Chung, S. H., and Buseck, P. R.: Shapes of soot aerosol particles and implications for their effects on climate, Journal of Geophysical Research: Atmospheres, 115, https://doi.org/10.1029/2009JD012868, 2010.

Alpert, P. A. and Knopf, D. A.: Analysis of isothermal and cooling-rate-dependent immersion freezing by a unifying stochastic ice nucleation model, Atmospheric Chemistry and Physics, 16, 2083–2107, https://doi.org/10.5194/acp-16-2083-2016, 2016.

Alpert, P. A., Kilthau, W. P., O'Brien, R. E., Moffet, R. C., Gilles, M. K., Wang, B., Laskin, A., Aller, J. Y., and Knopf, D. A.: Ice-nucleating agents in sea spray aerosol identified and quantified with a holistic multimodal freezing model, Science Advances, 8, eabq6842, https://doi.org/10.1126/sciadv.abq6842, 2022.

Andreae, M. O. and Crutzen, P. J.: Atmospheric aerosols: Biogeochemical sources and role in atmospheric chemistry, Science, 276, 1052–1058, https://doi.org/10.1126/science.276.5315.1052, 1997.

Ansmann, A., Tesche, M., Althausen, D., Müller, D., Seifert, P., Freudenthaler, V., Heese, B., Wiegner, M., Pisani, G., Knippertz, P., et al.: Influence of Saharan dust on cloud glaciation in southern Morocco during the Saharan Mineral Dust Experiment, Journal of Geophysical Research: Atmospheres, 113, https://doi.org/10.1029/2007JD008785, 2008.

Arabas, S., Curtis, J. H., Silber, I., Fridlind, A., Knopf, D. A., West, M., and Riemer, N.: Immersion freezing in particle-based aerosol-cloud microphysics: a probabilistic perspective on singular and time-dependent models, Journal of Advances in Modeling Earth Systems, https://doi.org/10.1029/2024MS004770, 2025.

Baustian, K. J., Cziczo, D. J., Wise, M. E., Pratt, K. A., Kulkarni, G., Hallar, A. G., and Tolbert, M. A.: Importance of aerosol composition, mixing state, and morphology for heterogeneous ice nucleation: A combined field and laboratory approach, Journal of Geophysical Research: Atmospheres, 117, https://doi.org/10.1029/2011JD016784, 2012.

Berkemeier, T., Ammann, M., Mentel, T. F., Po¨schl, U., and Shiraiwa, M.: Organic nitrate contribution to new particle formation and growth in secondary organic aerosols from α-pinene ozonolysis, Environmental science & technology, 50, 6334–6342, https://doi.org/10.1021/acs.est.6b00961, 2016.

Bi, Y., Cabriolu, R., and Li, T.: Heterogeneous ice nucleation controlled by the coupling of surface crystallinity and surface hydrophilicity, The Journal of Physical Chemistry C, 120, 1507–1514, https://doi.org/10.1021/acs.jpcc.5b09740, 2016.

Broadley, S., Murray, B., Herbert, R., Atkinson, J., Dobbie, S., Malkin, T., Condliffe, E., and Neve, L.: Immersion mode heterogeneous ice nucleation by an illite rich powder representative of atmospheric mineral dust, Atmospheric Chemistry and Physics, 12, 287–307, https://doi.org/10.5194/acp-12-287-2012, 2012.

Charnawskas, J. C., Alpert, P. A., Lambe, A. T., Berkemeier, T., O'Brien, R. E., Massoli, P., Onasch, T. B., Shiraiwa, M., Moffet, R. C., Gilles, M. K., et al.: Condensed-phase biogenic–anthropogenic interactions with implications for cold cloud formation, Faraday discussions, 200, 165–194, https://doi.org/10.1039/c7fd00010c, 2017.

Ching, J., Riemer, N., and West, M.: Impacts of black carbon mixing state on black carbon nucleation scavenging: Insights from a particle-resolved model, Journal of Geophysical Research: Atmospheres, 117, https://doi.org/10.1029/2012JD018269, 2012.

Chou, C., Formenti, P., Maille, M., Ausset, P., Helas, G., Harrison, M., and Osborne, S.: Size distribution, shape, and composition of mineral dust aerosols collected during the African Monsoon Multidisciplinary Analysis Special Observation Period 0: Dust

https://doi.org/10.5194/egusphere-2025-4326
Preprint. Discussion started: 24 September 2025

and Biomass-Burning Experiment field campaign in Niger, January 2006, Journal of Geophysical Research: Atmospheres, 113, https://doi.org/10.1029/2008JD009897, 2008.

Conny, J. M. and Buseck, P. R.: Microanalysis of Atmospheric Particles: Techniques and Applications, John Wiley & Sons, https://doi.org/10.1002/9781119554318, 2024.

Consiglio, A. N., Ouyang, Y., Powell-Palm, M. J., and Rubinsky, B.: An extreme value statistics model of heterogeneous ice nucleation for quantifying the stability of supercooled aqueous systems, The Journal of Chemical Physics, 159, https://doi.org/10.1063/5.0155494, 2023.

Curtis, J. H., Michelotti, M., Riemer, N., Heath, M. T., and West, M.: Accelerated simulation of stochastic particle removal processes in particle-resolved aerosol models, Journal of Computational Physics, 322, 21–32, https://doi.org/10.1016/j.jcp.2016.06.029, 2016.

Curtis, J. H., Riemer, N., and West, M.: A single-column particle-resolved model for simulating the vertical distribution of aerosol mixing state: WRF-PartMC-MOSAIC-SCM v1. 0, Geoscientific Model Development, 10, 4057–4079, https://doi.org/10.5194/gmd-10-4057-2017, 2017.

Deng, Z., Zhao, C., Ma, N., Ran, L., Zhou, G., Lu, D., and Zhou, X.: An examination of parameterizations for the CCN number concentration based on in situ measurements of aerosol activation properties in the North China Plain, Atmospheric Chemistry and Physics, 13, 6227–6237, https://doi.org/10.5194/acp-13-6227-2013, 2013.

DeVille, L., Riemer, N., and West, M.: Convergence of a generalized Weighted Flow Algorithm for stochastic particle coagulation, Journal of Computational Dynamics, 6, 69–94, https://doi.org/10.3934/jcd.2019003, 2019.

DeVille, R. L., Riemer, N., and West, M.: Weighted Flow Algorithms (WFA) for stochastic particle coagulation, Journal of Computational Physics, 230, 8427–8451, https://doi.org/10.1016/j.jcp.2011.07.027, 2011.

Dick, W. D., Ziemann, P. J., Huang, P.-F., and McMurry, P. H.: Optical shape fraction measurements of submicrometre laboratory and atmospheric aerosols, Measurement Science and Technology, 9, 183, https://doi.org/10.1088/0957-0233/9/2/006, 1998.

Diehl, K. and Mitra, S.: A laboratory study of the effects of a kerosene-burner exhaust on ice nucleation and the evaporation rate of ice crystals, Atmospheric Environment, 32, 3145–3151, https://doi.org/10.1016/S1352-2310(97)00467-6, 1998.

Fitzner, M., Sosso, G. C., Cox, S. J., and Michaelides, A.: The many faces of heterogeneous ice nucleation: Interplay between surface morphology and hydrophobicity, Journal of the American Chemical Society, 137, 13 658–13 669, https://doi.org/10.1021/jacs.5b08748, 2015.

Fletcher, N. H.: Size effect in heterogeneous nucleation, The Journal of chemical physics, 29, 572–576, https://doi.org/10.1063/1.1744540, 1958.

Fletcher, N. H.: On ice-crystal production by aerosol particles, Journal of Atmospheric Sciences, 16, 173–180, https://doi.org/10.1175/1520-0469(1959)016<0173:OICPBA>2.0.CO;2, 1959.

Fletcher, N. H.: Surface structure of water and ice, Philosophical Magazine, 7, 255–269, https://doi.org/10.1080/14786436208211860, 1962.

Hodshire, A. L., Akherati, A., Alvarado, M. J., Brown-Steiner, B., Jathar, S. H., Jimenez, J. L., Kreidenweis, S. M., Lonsdale, C. R., Onasch, T. B., Ortega, A. M., et al.: Aging effects on biomass burning aerosol mass and composition: A critical review of field and laboratory studies, Environmental science & technology, 53, 10 007–10 022, https://doi.org/10.1021/acs.est.9b02588, 2019.

Hoose, C. and Möhler, O.: Heterogeneous ice nucleation on atmospheric aerosols: a review of results from laboratory experiments, Atmospheric Chemistry and Physics, 12, 9817–9854, https://doi.org/10.5194/acp-12-9817-2012, 2012.

Hughes, M., Kodros, J. K., Pierce, J. R., West, M., and Riemer, N.: Machine learning to predict the global distribution of aerosol mixing state metrics, Atmosphere, 9, 15, https://doi.org/10.3390/atmos9010015, 2018.

https://doi.org/10.5194/egusphere-2025-4326
Preprint. Discussion started: 24 September 2025

Joghataei, M., Ostovari, F., Atabakhsh, S., and Tobeiha, N.: Heterogeneous ice nucleation by Graphene nanoparticles, Scientific Reports, 10, 9723, https://doi.org/10.1038/s41598-020-66714-2, 2020.

Kaiser, J., Riemer, N., and Knopf, D.: Detailed heterogeneous oxidation of soot surfaces in a particle-resolved aerosol model, Atmospheric Chemistry and Physics, 11, 4505–4520, https://doi.org/10.5194/acp-11-4505-2011, 2011.

Kanji, Z. A., Ladino, L. A., Wex, H., Boose, Y., Burkert-Kohn, M., Cziczo, D. J., and Krämer, M.: Overview of ice nucleating particles, Meteorological monographs, 58, 1–1, https://doi.org/10.1175/AMSMONOGRAPHS-D-16-0006.1, 2017.

Kiselev, A., Bachmann, F., Pedevilla, P., Cox, S. J., Michaelides, A., Gerthsen, D., and Leisner, T.: Active sites in heterogeneous ice nucleation—the example of K-rich feldspars, Science, 355, 367–371, https://doi.org/10.1126/science.aai8034, 2017.

Knopf, D., Barry, K., Brubaker, T., Jahl, L., Jankowski, K., Li, J., Lu, Y., Monroe, L., Moore, K., Rivera-Adorno, F., et al.: Aerosol–ice formation closure: a southern great plains field campaign, Bulletin of the American meteorological society, 102, E1952–E1971, https://doi.org/10.1175/BAMS-D-20-0151.1, 2021.

Knopf, D. A. and Alpert, P. A.: A water activity based model of heterogeneous ice nucleation kinetics for freezing of water and aqueous solution droplets, Faraday discussions, 165, 513–534, https://doi.org/10.1039/C3FD00035D, 2013.

Knopf, D. A. and Alpert, P. A.: Atmospheric ice nucleation, Nature Reviews Physics, 5, 203–217, https://doi.org/10.1038/s42254-023-00570-7, 2023.

Knopf, D. A., Alpert, P. A., Wang, B., O'Brien, R. E., Kelly, S. T., Laskin, A., Gilles, M. K., and Moffet, R. C.: Microspectroscopic imaging and characterization of individually identified ice nucleating particles from a case field study, Journal of Geophysical Research: Atmospheres, 119, 10–365, https://doi.org/10.1002/2014JD021866, 2014.

Knopf, D. A., Alpert, P. A., and Wang, B.: The role of organic aerosol in atmospheric ice nucleation: a review, ACS Earth and Space Chemistry, 2, 168–202, https://doi.org/10.1021/acsearthspacechem.7b00120, 2018.

Knopf, D. A., Alpert, P. A., Zipori, A., Reicher, N., and Rudich, Y.: Stochastic nucleation processes and substrate abundance explain time-dependent freezing in supercooled droplets, NPJ climate and atmospheric science, 3, 2, https://doi.org/10.1038/s41612-020-0106-4, 2020.

Knopf, D. A., Wang, P., Wong, B., Tomlin, J. M., Veghte, D. P., Lata, N. N., China, S., Laskin, A., Moffet, R. C., Aller, J. Y., et al.: Physicochemical characterization of free troposphere and marine boundary layer ice-nucleating particles collected by aircraft in the eastern North Atlantic, Atmospheric Chemistry and Physics, 23, 8659–8681, https://doi.org/10.5194/egusphere-2023-559, 2023.

Koop, T., Luo, B., Biermann, U. M., Crutzen, P. J., and Peter, T.: Freezing of HNO3/H2SO4/H2O solutions at stratospheric temperatures: Nucleation statistics and experiments, The Journal of Physical Chemistry A, 101, 1117–1133, https://doi.org/10.1021/jp9626531, 1997.

Koop, T., Luo, B., Tsias, A., and Peter, T.: Water activity as the determinant for homogeneous ice nucleation in aqueous solutions, Nature, 406, 611–614, https://doi.org/10.1038/35020537, 2000.

Laskin, A., Gilles, M. K., Knopf, D. A., Wang, B., and China, S.: Progress in the analysis of complex atmospheric particles, Annual Review of Analytical Chemistry, 9, 117–143, https://doi.org/10.1146/annurev-anchem-071015-041521, 2016.

Laskin, A., Moffet, R. C., and Gilles, M. K.: Chemical imaging of atmospheric particles, Accounts of Chemical Research, 52, 3419–3431, https://doi.org/10.1021/acs.accounts.9b00396, 2019.

Lata, N. N., Zhang, B., Schum, S., Mazzoleni, L., Brimberry, R., Marcus, M. A., Cantrell, W. H., Fialho, P., Mazzoleni, C., and China, S.: Aerosol composition, mixing state, and phase state of free tropospheric particles and their role in ice cloud formation, ACS Earth and Space Chemistry, 5, 3499–3510, https://doi.org/10.1021/acsearthspacechem.1c00315, 2021.

Leonard, J. and Im, J. S.: Modelling solid nucleation and growth in supercooled liquid, MRS Online Proceedings Library (OPL), 580, 233, https://doi.org/10.1557/PROC-580-233, 1999.

https://doi.org/10.5194/egusphere-2025-4326
Preprint. Discussion started: 24 September 2025

Lesins, G., Chylek, P., and Lohmann, U.: A study of internal and external mixing scenarios and its effect on aerosol optical properties and direct radiative forcing, Journal of Geophysical Research: Atmospheres, 107, AAC–5, https://doi.org/10.1029/2001JD000973, 2002.

Liu, L. and Mishchenko, M.: Scattering and radiative properties of morphologically complex carbonaceous aerosols: A systematic modeling study, Remote Sens., 10, 1634, https://doi.org/10.3390/rs10101634, 2018.

Lohmann, U.: Possible aerosol effects on ice clouds via contact nucleation, Journal of the atmospheric sciences, 59, 647–656, https://doi.org/10.1175/1520-0469(2001)059<0647:PAEOIC>2.0.CO;2, 2002.

Ma, N., Zhao, C., Nowak, A., Müller, T., Pfeifer, S., Cheng, Y., Deng, Z., Liu, P., Xu, W., Ran, L., et al.: Aerosol optical properties in the North China Plain during HaChi campaign: an in-situ optical closure study, Atmospheric Chemistry and Physics, 11, 5959–5973, https://doi.org/10.5194/acp-11-5959-2011, 2011.

Ma, N., Zhao, C., Müller, T., Cheng, Y., Liu, P., Deng, Z., Xu, W., Ran, L., Nekat, B., Van Pinxteren, D., et al.: A new method to determine the mixing state of light absorbing carbonaceous using the measured aerosol optical properties and number size distributions, Atmospheric Chemistry and Physics, 12, 2381–2397, https://doi.org/10.5194/acp-12-2381-2012, 2012.

McCoy, D. T., Hartmann, D. L., and Grosvenor, D. P.: Observed Southern Ocean cloud properties and shortwave reflection. Part I: Calculation of SW flux from observed cloud properties, Journal of Climate, 27, 8836–8857, https://doi.org/10.1175/JCLI-D-14-00287.1, 2014a.

McCoy, D. T., Hartmann, D. L., and Grosvenor, D. P.: Observed Southern Ocean cloud properties and shortwave reflection. Part II: Phase changes and low cloud feedback, Journal of Climate, 27, 8858–8868, https://doi.org/10.1175/JCLI-D-14-00288.1, 2014b.

McCoy, D. T., Tan, I., Hartmann, D. L., Zelinka, M. D., and Storelvmo, T.: On the relationships among cloud cover, mixed-phase partitioning, and planetary albedo in GCMs, Journal of Advances in Modeling Earth Systems, 8, 650–668, https://doi.org/10.1002/2015MS000589, 2016.

Michelotti, M., Heath, M. T., and West, M.: Binning for efficient stochastic multiscale particle simulations, Multiscale Modeling & Simulation, 11, 1071–1096, https://doi.org/10.1137/130908038, 2013.

Möhler, O., Benz, S., Saathoff, H., Schnaiter, M., Wagner, R., Schneider, J., Walter, S., Ebert, V., and Wagner, S.: The effect of organic coating on the heterogeneous ice nucleation efficiency of mineral dust aerosols, Environmental Research Letters, 3, 025 007, https://doi.org/10.1088/1748-9326/3/2/025007, 2008.

Murphy, D. and Thomson, D.: Chemical composition of single aerosol particles at Idaho Hill: Negative ion measurements, Journal of Geophysical Research: Atmospheres, 102, 6353–6368, https://doi.org/10.1029/96JD00859, 1997.

Murray, B., O'sullivan, D., Atkinson, J., and Webb, M.: Ice nucleation by particles immersed in supercooled cloud droplets, Chemical Society Reviews, 41, 6519–6554, https://doi.org/10.1039/C2CS35200A, 2012.

Murray, B. J., Carslaw, K. S., and Field, P. R.: Opinion: Cloud-phase climate feedback and the importance of ice-nucleating particles, Atmospheric Chemistry and Physics, 21, 665–679, https://doi.org/10.5194/acp-21-665-2021, 2021.

Niedermeier, D., Augustin-Bauditz, S., Hartmann, S., Wex, H., Ignatius, K., and Stratmann, F.: Can we define an asymptotic value for the ice active surface site density for heterogeneous ice nucleation?, Journal of Geophysical Research: Atmospheres, 120, 5036–5046, https://doi.org/10.1002/2014JD022814, 2015.

Phillips, V. T., DeMott, P. J., and Andronache, C.: An empirical parameterization of heterogeneous ice nucleation for multiple chemical species of aerosol, Journal of the atmospheric sciences, 65, 2757–2783, https://doi.org/10.1175/2007JAS2546.1, 2008.

Pruppacher, H. R. and Klett, J. D.: Microphysics of Clouds and Precipitation, Reidel, Dordrecht, https://doi.org/10.1080/02786829808965531, 1979.

https://doi.org/10.5194/egusphere-2025-4326
Preprint. Discussion started: 24 September 2025

Rejano, F., Casans, A., Via, M., Casquero-Vera, J. A., Castillo, S., Lyamani, H., Cazorla, A., Andrews, E., Pérez-Ramírez, D., Alastuey, A., et al.: CCN estimations at a high-altitude remote site: role of organic aerosol variability and hygroscopicity, Atmospheric Chemistry and Physics, 24, 13 865–13 888, https://doi.org/10.5194/acp-24-13865-2024, 2024.

Ren, J., Zhang, F., Wang, Y., Collins, D., Fan, X., Jin, X., Xu, W., Sun, Y., Cribb, M., and Li, Z.: Using different assumptions of aerosol mixing state and chemical composition to predict CCN concentrations based on field measurements in urban Beijing, Atmospheric Chemistry and Physics, 18, 6907–6921, https://doi.org/10.5194/acp-18-6907-2018, 2018.

Riemer, N. and West, M.: Quantifying aerosol mixing state with entropy and diversity measures, Atmospheric Chemistry and Physics, 13, 11 423–11 439, https://doi.org/10.5194/acp-13-11423-2013, 2013.

Riemer, N., West, M., Zaveri, R. A., and Easter, R. C.: Simulating the evolution of soot mixing state with a particle-resolved aerosol model, Journal of Geophysical Research: Atmospheres, 114, https://doi.org/10.1029/2008JD011073, 2009.

Rudich, Y.: Laboratory perspectives on the chemical transformations of organic matter in atmospheric particles, Chemical Reviews, 103, 5097–5124, https://doi.org/10.1021/cr020508f, 2003.

Shao, Y., Voliotis, A., Du, M., Wang, Y., Pereira, K., Hamilton, J., Alfarra, M. R., and McFiggans, G.: Chemical composition of secondary organic aerosol particles formed from mixtures of anthropogenic and biogenic precursors, Atmospheric Chemistry and Physics, 22, 9799–9826, https://doi.org/10.5194/acp-22-9799-2022, 2022.

Shima, S.-i., Sato, Y., Hashimoto, A., and Misumi, R.: Predicting the morphology of ice particles in deep convection using the super-droplet method: Development and evaluation of SCALE-SDM 0.2. 5-2.2. 0,-2.2. 1, and-2.2. 2, Geoscientific Model Development, 13, 4107–4157, https://doi.org/10.5194/gmd-13-4107-2020, 2020.

Spichtinger, P. and Cziczo, D. J.: Impact of heterogeneous ice nuclei on homogeneous freezing events in cirrus clouds, Journal of Geophysical Research: Atmospheres, 115, https://doi.org/10.1029/2009JD012168, 2010.

Stevens, R. and Dastoor, A.: A review of the representation of aerosol mixing state in atmospheric models, Atmosphere, 10, 168, https://doi.org/10.3390/atmos10040168, 2019.

Storelvmo, T.: Aerosol effects on climate via mixed-phase and ice clouds, Annual Review of Earth and Planetary Sciences, 45, 199–222, https://doi.org/10.1146/annurev-earth-060115-012240, 2017.

Sullivan, R., Petters, M. D., DeMott, P. J., Kreidenweis, S. M., Wex, H., Niedermeier, D., Hartmann, S., Clauss, T., Stratmann, F., Reitz, P., et al.: Irreversible loss of ice nucleation active sites in mineral dust particles caused by sulphuric acid condensation, Atmospheric Chemistry and Physics, 10, 11 471–11 487, https://doi.org/10.5194/acp-10-11471-2010, 2010.

Szakáll, M., Debertshäuser, M., Lackner, C., Mayer, A., Eppers, O., Diehl, K., Theis, A., Mitra, S., and Borrmann, S.: Comparative study on immersion freezing utilizing single-droplet levitation methods, Atmospheric Chemistry and Physics, 21, 3289–3316, https://doi.org/10.5194/acp-21-3289-2021, 2021.

Tian, J., Riemer, N., West, M., Pfaffenberger, L., Schlager, H., and Petzold, A.: Modeling the evolution of aerosol particles in a ship plume using PartMC-MOSAIC, Atmospheric chemistry and physics, 14, 5327–5347, https://doi.org/10.5194/acp-14-5327-2014, 2014.

Valsan, A. E., Ravikrishna, R., Biju, C., Pöhlker, C., Després, V., Huffman, J., Pöschl, U., and Gunthe, S.: Fluorescent biological aerosol particle measurements at a tropical high-altitude site in southern India during the southwest monsoon season, Atmospheric Chemistry and Physics, 16, 9805–9830, https://doi.org/10.5194/acp-16-9805-2016, 2016.

Wagner, R., Ickes, L., Bertram, A. K., Els, N., Gorokhova, E., Möhler, O., Murray, B. J., Umo, N. S., and Salter, M. E.: Heterogeneous ice nucleation ability of aerosol particles generated from Arctic sea surface microlayer and surface seawater samples at cirrus temperatures, Atmospheric Chemistry and Physics, 21, 13 903–13 930, https://doi.org/10.5194/acp-21-13903-2021, 2021.

https://doi.org/10.5194/egusphere-2025-4326
Preprint. Discussion started: 24 September 2025

Wang, B., Knopf, D. A., China, S., Arey, B. W., Harder, T. H., Gilles, M. K., and Laskin, A.: Direct observation of ice nucleation events on individual atmospheric particles, Physical Chemistry Chemical Physics, 18, 29 721–29 731, https://doi.org/10.1039/c6cp05253c, 2016.

Wang, Y., Li, Z., Zhang, Y., Du, W., Zhang, F., Tan, H., Xu, H., Fan, T., Jin, X., Fan, X., et al.: Characterization of aerosol hygroscopicity, mixing state, and CCN activity at a suburban site in the central North China Plain, Atmospheric Chemistry and Physics, 18, 11 739–11 752, https://doi.org/10.5194/acp-18-11739-2018, 2018.

Winkler, P.: The growth of atmospheric aerosol particles as a function of the relative humidity—II. An improved concept of mixed nuclei, Journal of Aerosol Science, 4, 373–387, https://doi.org/10.1016/0021-8502(73)90027-X, 1973.

Xue, J., Zhang, T., Park, K., Yan, J., Yoon, Y. J., Park, J., and Wang, B.: Diverse sources and aging change the mixing state and ice nucleation properties of aerosol particles over the western Pacific and Southern Ocean, Atmospheric Chemistry and Physics, 24, 7731–7754, https://doi.org/10.5194/acp-24-7731-2024, 2024.

Yang, F., Cruikshank, O., He, W., Kostinski, A., and Shaw, R. A.: Nonthermal ice nucleation observed at distorted contact lines of supercooled water drops, Physical Review E, 97, 023 103, https://doi.org/10.1103/PhysRevE.97.023103, 2018.

Yao, Y., Curtis, J. H., Ching, J., Zheng, Z., and Riemer, N.: Quantifying the effects of mixing state on aerosol optical properties, Atmospheric Chemistry and Physics, 22, 9265–9282, https://doi.org/10.5194/acp-22-9265-2022, 2022.

Zaveri, R. A., Easter, R. C., Fast, J. D., and Peters, L. K.: Model for simulating aerosol interactions and chemistry (MOSAIC), Journal of Geophysical Research: Atmospheres, 113, https://doi.org/10.1029/2007JD008782, 2008.

Zhang, Q., Jimenez, J. L., Canagaratna, M., Allan, J. D., Coe, H., Ulbrich, I., Alfarra, M., Takami, A., Middlebrook, A., Sun, Y., et al.: Ubiquity and dominance of oxygenated species in organic aerosols in anthropogenically-influenced Northern Hemisphere midlatitudes, Geophysical research letters, 34, https://doi.org/10.1029/2007GL029979, 2007.

Zheng, Z., West, M., Zhao, L., Ma, P.-L., Liu, X., and Riemer, N.: Quantifying the structural uncertainty of the aerosol mixing state representation in a modal model, Atmospheric Chemistry and Physics, 21, 17 727–17 741, https://doi.org/10.5194/acp-21-17727-2021, 2021.

Zuberi, B., Bertram, A. K., Cassa, C. A., Molina, L. T., and Molina, M. J.: Heterogeneous nucleation of ice in (NH4) 2SO4-H2O particles with mineral dust immersions, Geophysical research letters, 29, 142–1, https://doi.org/10.1029/2001GL014289, 2002.